GRADUATE AERONAUTICAL LABORATORIES
CALIFORNIA INSTITUTE OF TECHNOLOGY

Aerodynamic Control and Mixing with Ramp Injection

MICHAEL BERNARD JOHNSON

2005

Firestone Flight Sciences Laboratory

Guggenheim Aeronautical Laboratory

Karman Laboratory of Fluid Mechanics and Jet Propulsion

Pasadena

Aerodynamic Control and Mixing with Ramp Injection

Thesis by

Michael Bernard Johnson

In Partial Fulfillment of the Requirements

for the Degree of

Engineer

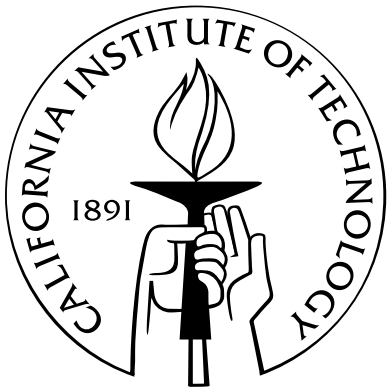

California Institute of Technology

Pasadena, California

2005

(Submitted May 25, 2005)

Acknowledgements

I would like to acknowledge the following people:

- Prof. Paul Dimotakis, for his guidance and support throughout this project.
- Erik Iglesias, Jeff Bergthorson and Georgios Matheou for their help and suggestions.
- Garrett Katzenstein, for his design ideas and help with running experiments.
- Dan Lang, whose help with computing and digital imaging was invaluable.
- Earl Dahl, without whom none of these experiments would have been possible.
- Wei-Jen Su, who was instrumental in helping me to learn the operation of the S^3L facility.
- Christina Mojahedi, for her extremely capable administrative support.
- Richard Germond and his capable staff at Caltech Physical Plant, who were always immensely helpful keeping the lab supplied with gases and other supplies for our experiments.
- Joe Haggerty, Bradley St. John and Ali Kiani from the Aeronautics machine shop, who were always willing to help and lend advice with design ideas and machining.

This work was funded by the Air Force Office of Scientific Research, Grant Nos. F49620-98-1-0052, F49620-01-1-0006 and FA9550-04-1-0020, under the supervision of Dr. Julian Tishkoff. Their support is acknowledged and greatly appreciated.

Abstract

Experiments have been conducted in the GALCIT Supersonic Shear Layer Facility (S^3L) to investigate the behaviour of a flow and geometry with many features that are potentially useful for a Supersonic Combustion Ramjet (SCRAMJET) engine — a recirculation zone for flameholding, enhanced mixing between fuel and air, and low total-pressure losses. In a subsonic diffuser configuration with no mass injection, the exit velocity and guidewall static-pressure profiles collapse over a large range of inlet Reynolds numbers. Significant control of exit velocity and guidewall pressure profiles is possible via injection through a perforated ramp into the freestream. The control authority on the overall pressure coefficient increases with increasing inlet Reynolds number. Simple control volume models put bounds on the overall pressure coefficient for the device.

In low-supersonic flow, the area ratio calculated from measured pressures agrees well with the visual shear-layer thickness, illustrating the low total-pressure losses present.

Further control is possible through variable heat release from a fast-chemical reaction between reactants carried in the two streams. At the highest heat release studied, mass injection requirements are lowered by, roughly, a factor of two. Measurements of mixing inferred from the temperature rise from such a reaction indicate a high level of mixing vs. classical free shear layers. As in free shear layers, however, the level of mixing begins to decrease with increasing heat release.

Contents

Chapter 1

Introduction

A successful fuel injection scheme for a Supersonic Combustion Ramjet (SCRAMJET) engine must provide rapid mixing of fuel and air, and a low strain-rate flameholding region to keep the flame lit, while not incurring unacceptably large total-pressure losses.

The simplest geometry is normal injection of fuel from a wall orifice (Ben-Yakar and Hanson, 2001). A bow shock is produced upstream of the injection port, causing the boundary layer to separate, and creating a flameholding region where jet and boundary-layer fluids mix subsonically. This method suffers total-pressure losses due to the 3-dimensional bow shock upstream of the injection port that may be unacceptable. Angled injection, while reducing total-pressure losses and contributing to the net engine thrust, can result in reduced mixing and flameholding benefits.

Addition of a cavity downstream of the injection port can increase flameholding by creating a recirculation zone inside the cavity with a hot pool of radicals. However, at the end of the cavity is a step, which creates drag and large total-pressure losses. Inclined walls still increase drag and total-pressure losses in the combustor. Gruber et al. (2001), in their investigation of different cavity geometries at Mach 3, found that as the aft wall angle was made shallower, the drag coefficient actually increased due to higher pressures acting over a larger fraction of the aft wall area. Yu et al. (2001) found that there was a trade-off between cavity-enhanced mixing and combustion efficiency, and cavity-induced drag.

In many flows it is desirable to use variable geometry in order to adapt to a wide range of flow conditions, e.g., supersonic inlets. However, there is a significant penalty in weight and mechanical complexity associated with these systems.

This thesis follows work by Su (2001), based on design and test-section contributions to the S^3L by Slessor (1998), and explores a geometry with potential for SCRAMJET mixing and flameholding with low total-pressure losses. It also has the potential to provide many of the benefits of variable geometry flow control aerodynamically, thus alleviating the penalties of excessive weight and mechanical complexity. It consists of a perforated ramp inclined at 30 degrees to the incoming flow.

With a solid ramp installed, this geometry is similar to the backward-facing step, on which much

prior work has been done. Eaton and Johnston (1981) conducted a review of work on subsonic flow reattachment, looking at the effect of the state and thickness of the boundary-layer upstream of separation, the freestream turbulence level, streamwise pressure gradient, and aspect ratio. They compared profiles of turbulence intensity, reattachment length, Reynolds shear stress and mean velocity. Bradshaw and Wong (1972) also conducted a review of low-speed flows past various steps and fences. Westphal and Johnston (1984) studied reattachment downstream of a backward-facing step for a range of inlet boundary-layer thicknesses, velocities and vorticity levels. Sinha et al. (1981) measured reattachment length, static pressure, turbulence intensity and mean velocity downstream of backward-facing steps and cavities for laminar inlet flow. Narayanan et al. (1974) and Adams and Johnston (1988) investigated the static pressure profiles downstream of backward-facing steps of various heights. The reattachment of a separated flow is a three-dimensional process, and this was investigated by Ruderich and Fernholz (1986) and Jaroch and Fernholz (1989) for flow past a normal plate. They found large spanwise variations in reattachment length, static pressure, mean velocity and Reynolds stresses.

Chapter 2 contains an overview of the experimental facility and diagnostics employed during this investigation. Chapter 3 describes results for nonreacting flows, subsonic and supersonic, and Chapter 4 presents results for flows with variable heat release, including an investigation of mixing and the effects of heat release on the flowfield.

Chapter 2

Experimental Facility

2.1 Overview

The experiments described herein were conducted in the GALCIT Supersonic Shear Layer Laboratory (S^3L). This facility is a two-stream blow-down wind tunnel capable of delivering flows up to $M_1 \sim 3.2$ in the upper stream, and $M_2 \sim 1.3$ in the lower stream, with a nominal run time of between two and six seconds.

The unique aspect of the facility is that it has been designed to handle gases whose chemical reaction time scale can be made very short. Specifically, the upper stream can be seeded with hydrogen (H_2) and nitric oxide (NO) in a balance of diluents (helium, argon and nitrogen), and the lower stream seeded with fluorine (F_2) in diluents (Hall and Dimotakis, 1989; Hall, 1991). The overall reaction is $H_2 + F_2 \rightarrow 2\,HF$, with an adiabatic flame temperature rise, $\Delta T_f \approx 94\,K$ for a mixture of 1% H_2 in the upper stream and 1% F_2 in the lower stream, both diluted with N_2. The activation energy for the main chain branching reaction, $NO + F_2 \rightarrow NOF + F$ is $E_A/k_B T_r \approx 3.84$. In contrast, for methane combustion, the initiation reaction $CH_4 + M \rightarrow CH_3 + H + M$ has an activation energy, $E_A/k_B T_r \approx 178$. The $H_2/NO/F_2$ reaction system is called "hypergolic", as it requires no ignition source. By varying the reactant concentrations in each stream, the Damkohler number,

$$Da = \frac{\tau_{mix}}{\tau_{chem}} \tag{2.1}$$

the ratio of the mixing time scale to the chemical time scale, can be made large enough to ensure that all fluid that is molecularly mixed will react to completion.

Fig. 2.1 is an overall schematic of the facility. Generally, tanks supplying gas for the upper and lower streams are charged with the desired concentration of reactants and allowed to mix. Each stream flows through a metering valve into the test section where they mix and, for reacting flow experiments, burn. Pressures and temperatures are measured in the test section, and schlieren images are acquired to visualize the flow. The exhaust gases are then neutralized and vented.

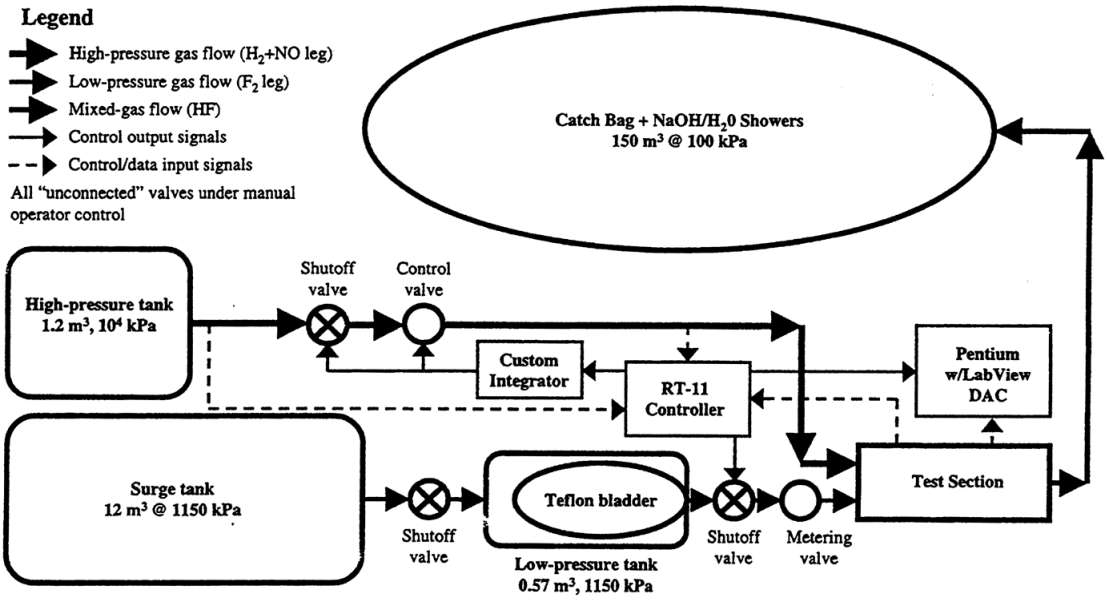

Figure 2.1: Schematic of overall facility gas-flow (from Slessor, 1998).

A summary of each aspect of the facility will be given below. More details can be found in Hall and Dimotakis (1989) and Hall (1991).

2.2 Upper Stream Gas Delivery

Gases for the upper stream are loaded directly from bottles into the H_2/NO Reactant Tank, using the partial pressure method to control the reactant concentrations. The tank has an internal volume of $1.2\,\mathrm{m}^3$ ($42\,\mathrm{ft}^3$), most of which is packed with two cylindrical rolls of aluminum mesh screen. This minimizes the temperature drop in the tank during blowdown operation, resulting in an approximately isothermal, as opposed to an isentropic blowdown. During the filling process, gases are injected along the central axis of the tank, which is free of screen. Thus, the gases rise along the axis and fall through the screens, ensuring complete mixing. After filling, the gases are allowed to settle and further mix for at least half an hour.

The experiment is started by opening the upper stream shutoff valve – a full-port ball valve (Valvtron) with an opening time of approximately 1 s. The upper stream gas then flows through a computer-controlled metering valve, an acoustic damping section and into the test section.

The computer controlled valve consists of a rotor and stator with matching slots. The angle between rotor and stator sets the effective area of the valve. For the experiments documented here, the valve was operated in essentially open-loop mode. The control computer measures the pressure in the reactant tank and, after an initial charge-up time, opens the valve at a constant rate, inversely

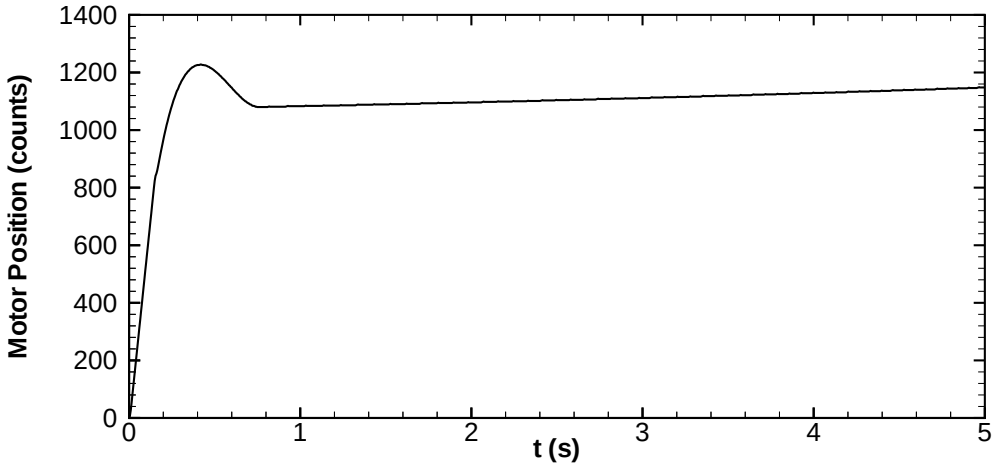

Figure 2.2: Sample trace of upper-stream computer controlled valve position during an experiment.

proportional to the pressure drop in the tank, thus maintaining the mass flux,

$$\dot{m} = A_{eff} p_t \sqrt{\frac{\gamma}{RT_t}} \left(\frac{\gamma+1}{2}\right)^{\frac{-(\gamma+1)}{2(\gamma-1)}} \tag{2.2}$$

constant during the experiment. Figure 2.2 shows a trace of the motor position during an experiment. As explained above, the aluminum mesh screen packing in the tank serves to hold the total temperature of the gas in the tank, T_t, nearly constant over the course of the experiment. For experiments with higher mass flux (*e.g.* supersonic upper stream), the valve is operated under feedback control. In this case, the upper-stream nozzle plenum pressure is also measured and the control system responds to maintain a user-specified rate of change over the course of the experiment.

2.3 Lower Stream Gas Delivery

Gas mixtures for the lower stream are first loaded into the F_2 Mixing Vessel, a 4.88 m (16 ft) long, 10 cm (4 in.) diameter pipe with a small perforated tube on its axis. Mixture compositions are controlled using the partial pressure method, as for the upper stream. Gases from the mixing vessel are transferred to a teflon bladder inside the F_2 Reactant Tank, a 0.57 m^3 (20 ft^3) volume vessel. The outside of the bladder is connected to the Surge Tank, with a volume of 12.7 m^3 (450 ft^3). Thus, during the experiment, the Surge Tank acts as a nearly-constant pressure source, squeezing the gas from the teflon bladder into the test section.

The shutoff valve for the lower stream is a globe valve with an opening time of approximately 0.5 s. The mass flux from the lower stream is set passively with a calibrated metering valve. The metering valve consists of two concentric cylinders, one with a helical array of 1/8 in. diameter holes.

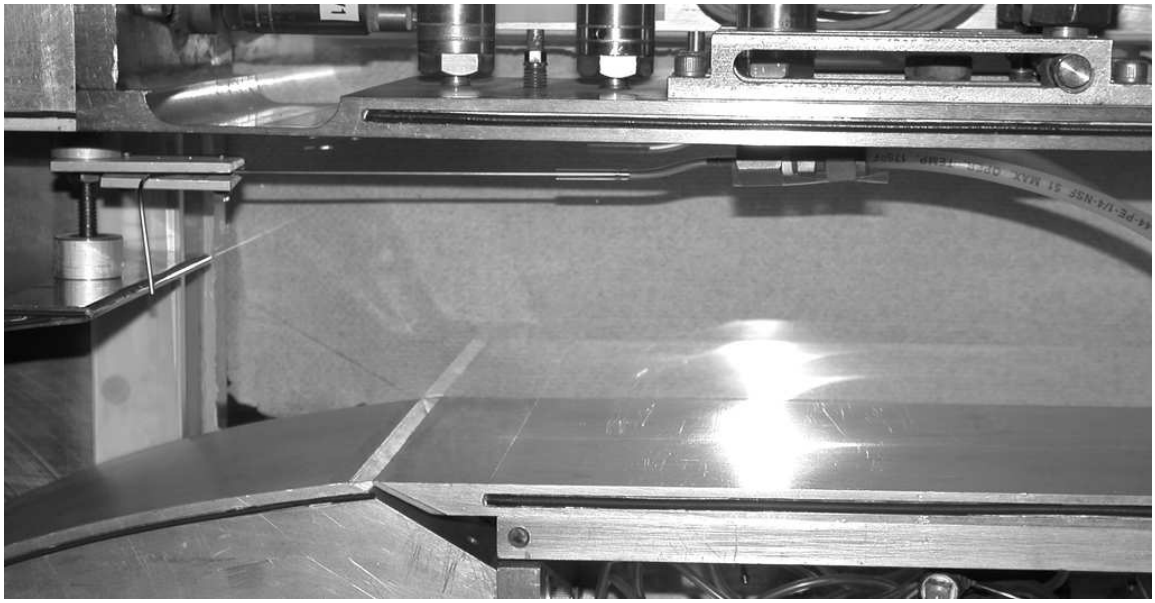

Figure 2.3: Photograph of setup used to calibrate the lower stream metering valve. Here the static pressure at the nozzle exit is sampled and routed to one side of a barocel pressure transducer, the other side of which was connected to the nozzle plenum.

Displacing the cylinders axially changes the number of holes exposed to the flow, thus setting the mass flux.

The valve was calibrated using the setup show in Fig. 2.3. The (Bernoulli) pressure difference between the plenum and exit of the lower stream nozzle was measured using a barocel pressure transducer (Edwards Model 570DF Barocel with Datametrics Model 1174 Electric Manometer). Converting this pressure difference to velocity using the standard formula

$$U = \sqrt{\frac{2\Delta p}{\rho\left[1 - \left(\frac{A_e}{A_i}\right)^2\right]}} \tag{2.3}$$

where A_e and A_i are the nozzle exit and inlet areas, yields the calibration curve shown in Fig. 2.4 for two surge tank pressures (p_0).

Downstream of this valve is a 7.5 cm (3 in.) thick stack of high-porosity aluminum mesh screen which serves to acoustically damp the lower stream flow before it enters the test section.

2.4 Test Section, Diagnostics and Data Acquisition

Figure 2.5 is a photograph of the S^3L test section. Upstream of the nozzle contractions seen on the left of this figure are the honeycomb and mesh screen sections through which each stream passes before entering their respective nozzles. The upper stream nozzle is removable, allowing for installation of

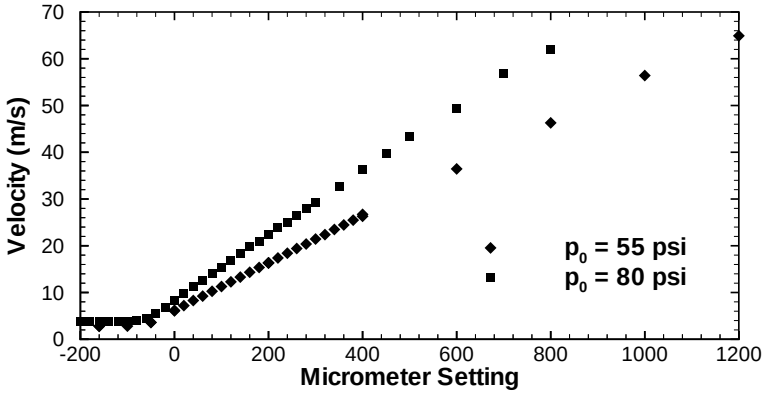

Figure 2.4: Lower stream nozzle velocity as a function of micrometer (metering valve) setting.

nozzles for different Mach numbers. The nozzle shown is optimized to deliver high-quality subsonic inflow.

The lower stream gas enters the test section through a perforated plate angled at 30 degrees to the upper stream flow. The details of the plate are shown in Fig. 2.6. It consists of 3611 0.062 in. diameter holes, yielding an open area ratio of approximately 65%. This value was chosen in order to avoid the jet-coalescence instability documented by Loehrke and Nagib (1972).

In the test section the upper and lower streams mix, forming a shear layer. At the exit of the test section is a rake of 16 total pressure probes and 16 thermocouples. Total pressures are measured with Druck Model PDCR 200 pressure transducers. Total temperatures are measured with Omega K Type chromel/alumel exposed-junction thermocouples. Figure 2.7 shows the details of the thermocouple construction. Static pressures on the upper guidewall are measured with Druck Model PDCR 900 absolute pressure transducers. Lower guidewall pressures are measured with Druck Model PMP 4411 differential pressure transducers, with all measuring stations referenced to the upper-stream inlet static pressure.

All channels are filtered and amplified before being sampled with LabView data acquisition software.

Schlieren visualizations were recorded with two imaging systems. The first is a 1024^2-pixel, 30 frames per second (fps) CCD camera (Silicon Mountain Design Model 1M30), used in conjunction with a Xenon Corporation Model N-789B Nanolamp and Model 437 Nanopulser driver unit. A schematic with this system employed is shown in Fig. 2.8. The other imaging system employed is the in-house designed "KFS" imaging system, a 1024^2-pixel CCD camera operated at 200 fps for these experiments, with a High-Speed Photo-Systeme "Nanolite" spark light source and "Mini-Strobokin" driver unit.

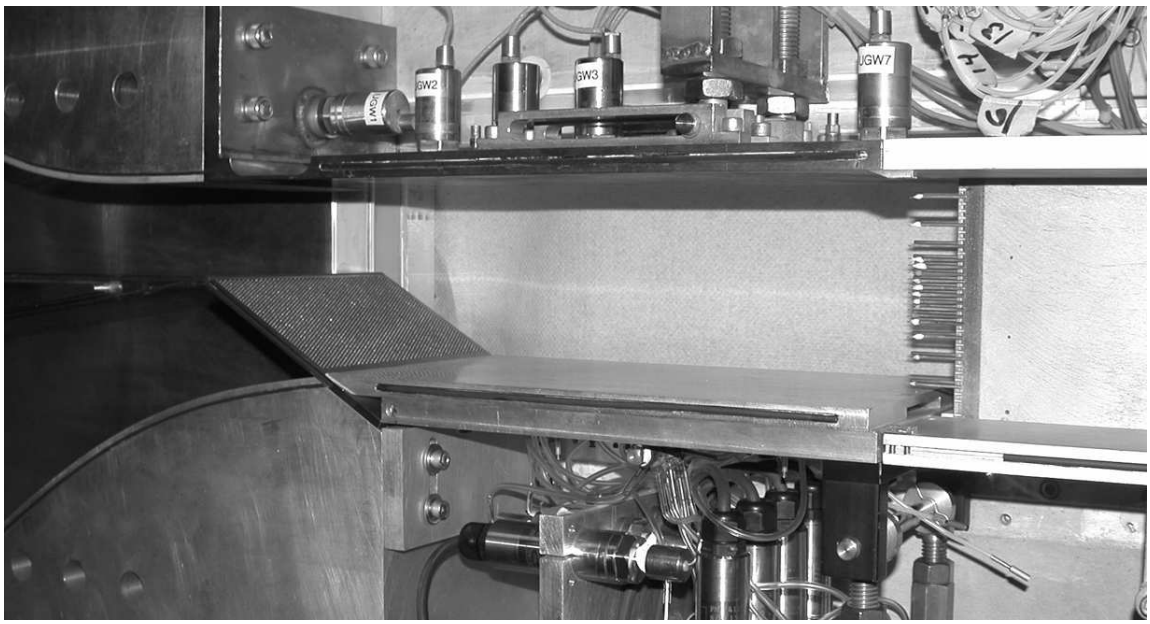

Figure 2.5: Photograph of the S^3L test section.

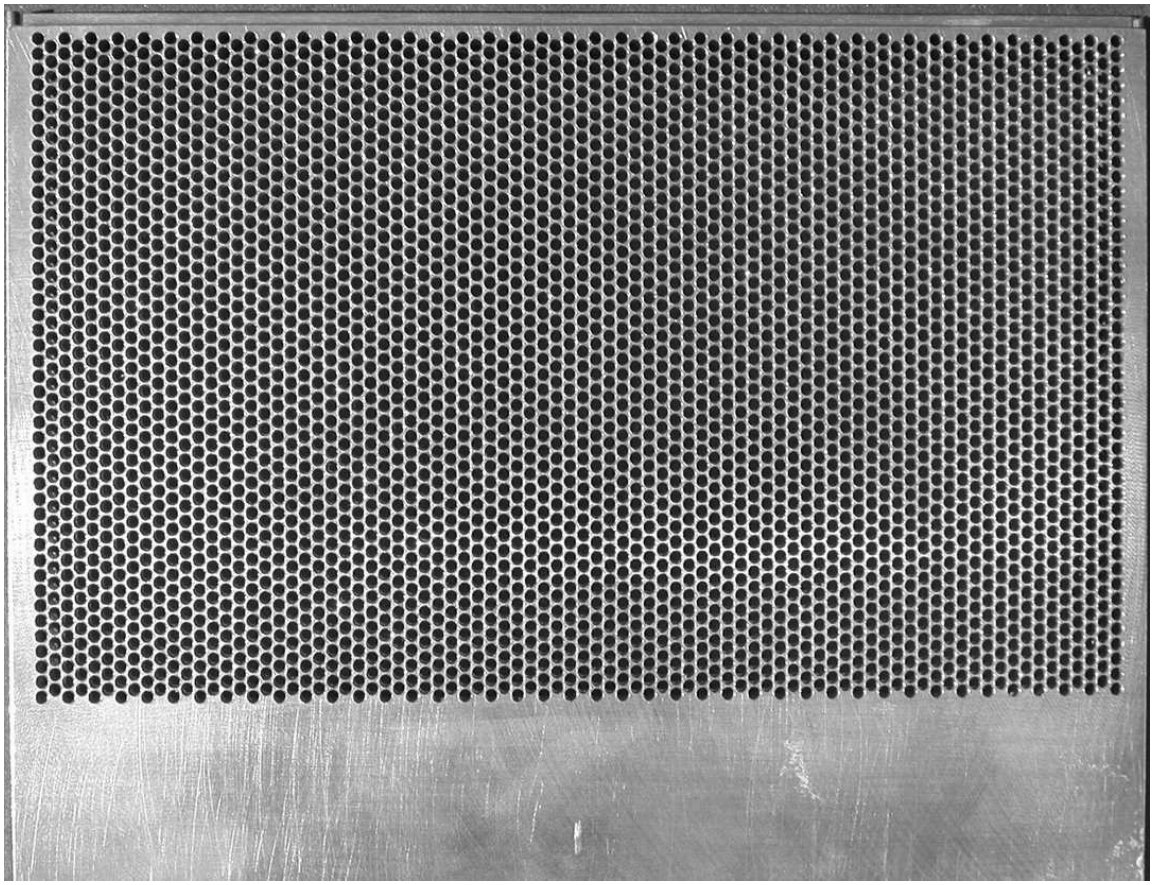

Figure 2.6: Photograph of the perforated plate used to inject the lower stream gas into the test section. Overall horizontal dimension is approximately 6 in.

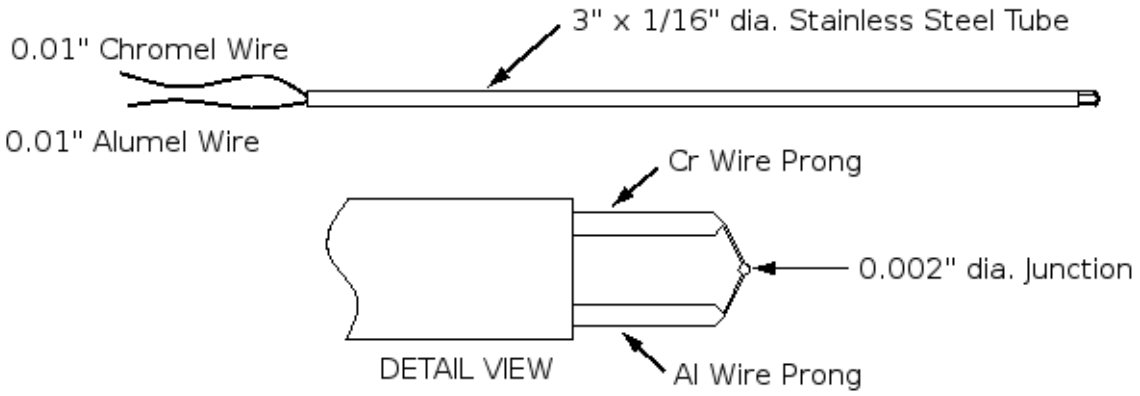

Figure 2.7: Detail of exposed-junction thermocouple probe construction.

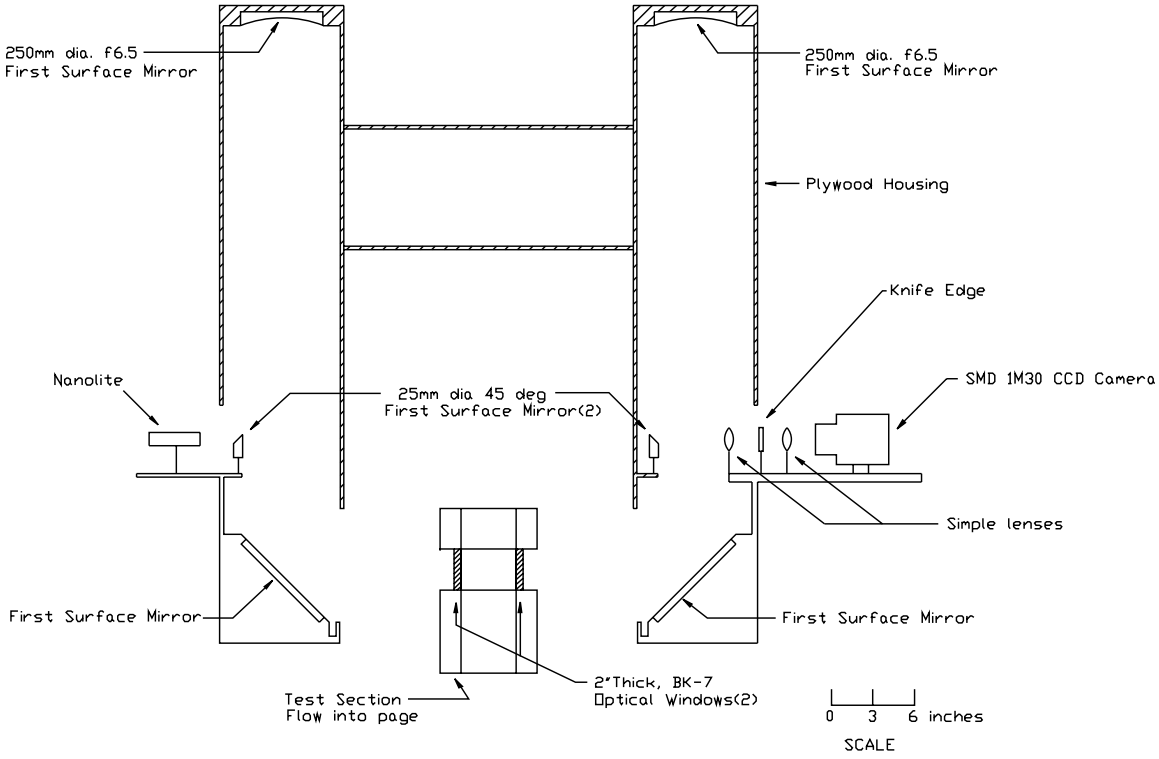

Figure 2.8: Schematic of S^{3}L schlieren system (adapted from Slessor, 1998).

2.5 Waste Gas Disposal

As the gases exit the test section they pass through a duct and into a large catch bag. During reacting experiments, the exhaust gases are sprayed with a fine mist of sodium hydroxide (NaOH) as they pass through the duct as well as in the catch bag. This cools the gases, and neutralizes the hydrofluoric acid (HF) formed from the reaction of H_2 and F_2. Excess gas from the upper stream reactant tank is vented into the catch bag and neutralized with the showers. The gas in the catch bag is then diluted to below flammability limits and vented.

Excess gas from the lower stream reactant tank and mixing vessel is vented through a bed of charcoal and bubbled through a tank of NaOH, neutralizing the unused F_2 gas.

2.6 Data Processing

Data from each experiment are truncated, removing the startup and shutdown periods, then divided into eight segments. An example of the upper-stream nozzle differential pressure acquired for a typical experiment is shown in Fig. 2.9. Data from this experiment would be truncated between approximately 2–3 s. Figure 2.10 shows the 8 segments of the temperature profile for this experiment. Overall statistics for each experiment represent a temporal average over the entire steady portion. To obtain engineering units (temperatures and pressures), offsets are subtracted from the raw data and the result is multiplied by the calibration constant for each sensor.

Test section exit velocity profiles are calculated from the total pressures as follows. For incompressible flow, the velocity is calculated directly from the total and static pressures,

$$U_e = \sqrt{2\,\frac{p_t\,(y) - p_s\,(y)}{\rho\,(y)}} \tag{2.4}$$

where p_t and p_s are the total and static pressures at the probe location. The static pressure, $p_s\,(y)$ is interpolated from the measurements at the upper and lower guidewall.

For compressible flows, the total pressures are first converted into Mach numbers,

$$M_e = \sqrt{\frac{2}{\gamma - 1}\left[\left(\frac{p_t}{p_s}\right)^{\frac{(\gamma-1)}{\gamma}} - 1\right]} \tag{2.5}$$

The static temperatures are calculated from the Mach number and measured total temperature,

$$T_s = \frac{T_t}{1 + \frac{\gamma-1}{2}M_e^2} \tag{2.6}$$

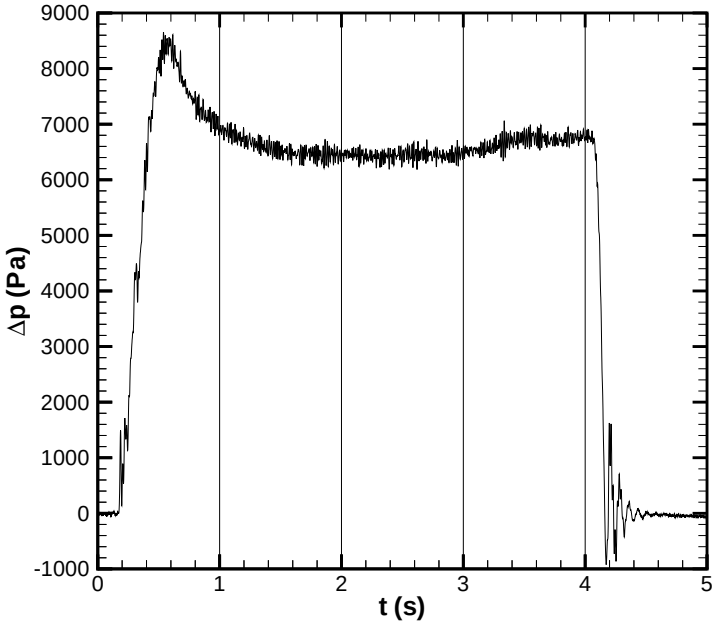

Figure 2.9: Upper-stream nozzle differential pressure during the course of a typical experiment, showing startup, steady flow, and shutdown periods.

Thus, the exit velocity is calculated,

$$U_e = M_e a_e = M_e \sqrt{\gamma R T_s} \tag{2.7}$$

The reacting flow experiments are always accompanied by a "cold-flow" experiment with the same velocity conditions and inert gas concentrations, but with no heat release. The temperature data from these experiments (typically a drop of order 5 K), are subtracted from the corresponding reacting experiment data to yield the temperature rise from the chemical reaction, ΔT.

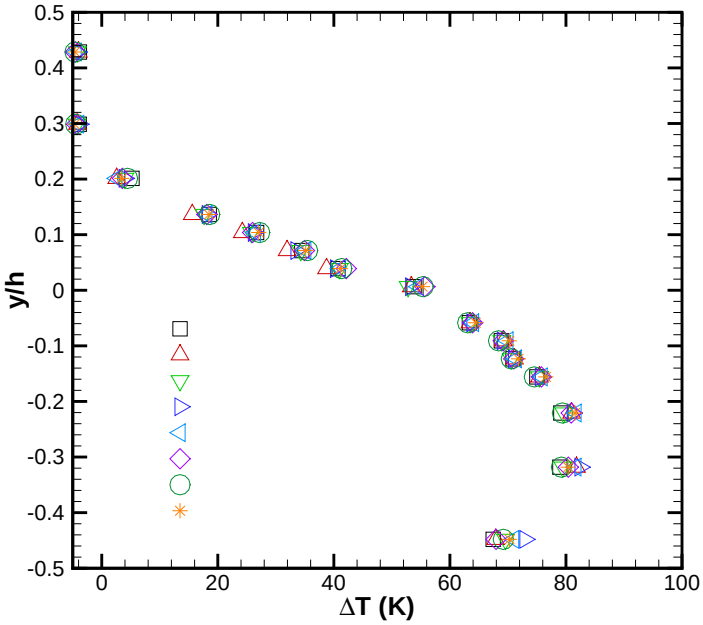

Figure 2.10: Example of temperature data split into 8 segments (legend shows symbol for each segment).

Chapter 3

Non-Reacting Flow

3.1 Flow Without Mass Injection

Experiments were conducted to investigate the behaviour of the flowfield and geometry under non-reacting conditions, with no mass injection. For these experiments, a solid ramp was installed in place of the perforated one described in Section 2.4 and shown in Fig. 2.6. This work is an extension of work done by Su (2001).

Figure 3.1 is a cartoon of the flow under these conditions. The flow enters the test section from the upper stream with velocity U_1. At the edge of the splitter plate, the flow separates over the ramp, and reattaches a distance x_R downstream, on the lower guidewall. As noted by Bradshaw and Wong (1972), a key feature of this flow is the reattachment, where part of the flow is deflected upstream into the recirculation zone to supply the entrainment requirements of the separating shear layer. As noted by Eaton and Johnston (1981), backflow velocities in the recirculation zone can reach over 20% of the freestream velocity, and the length of the separation region fluctuates as the reattachment point moves up and downstream.

Figure 3.2 plots the exit velocity and Fig. 3.3 plots the normalized exit velocity for the range of inlet velocities studied. It is seen that the normalized velocity profiles collapse well, with small Reynolds number effects near the lower wall. Figure 3.4 plots the exit velocity at the four lowest probe locations, versus the inlet velocity. At the lowest probe location, there is a slight decrease in exit velocity as the inlet velocity is increased.

If it were possible to measure the velocity profile at the reattachment point, $x = x_R$, one would expect that the velocity near the lower wall would be zero. This is the case in two of the experiments reviewed by Eaton and Johnston (1981). Upstream of the reattachment point, as mentioned above, there is backflow, and downstream of the reattachment point the flow relaxes and the profile becomes more uniform. Thus, Figs. 3.2 and 3.4 would seem to imply that the reattachment point in these experiments is moving slightly downstream (x_R increasing) as the inlet velocity and Reynolds number are increased. In contrast, Eaton and Johnston (1981) note that the reattachment length

decreases slightly with momentum thickness Reynolds number, for a transitional boundary layer, and is independent of Reynolds number when the boundary layer becomes fully turbulent. They give values of $x_R/h \sim 7.5 - 8$ for transitional/turbulent boundary layers. Kim et al. (1980) performed experiments at $Re_\theta \sim 1.3 \times 10^3$ and quote $x_R/h \sim 7 \pm 1$. For this flow, the upper-stream boundary layer before separation is estimated to be laminar up to $U_1 \approx 126\,\mathrm{m/s}$ and transitional/turbulent for higher inlet velocities. The overall dimension of the test section is $L/h = 7.84$, so if the reattachment point were near the probe location, x_R/h would not be too different from published results for flow over backward facing steps.

The location of the reattachment line can vary significantly in the spanwise direction. Jaroch and Fernholz (1989) investigated the three-dimensional nature of flow separating from a normal plate and found that the reattachment length can vary by as much as 50% from the centerline to the edge of the facility. Ruderich and Fernholz (1986) also noted large variations in mean velocity and reattachment length in the spanwise direction for flow separating from a normal plate. In numerical simulations of forced convection flow adjacent to a backward-facing step, Nie and Armaly (2003) found large spanwise variations of the reattachment line.

It should be noted that the flow in this geometry is slightly different from that reviewed as the presence of the ramp removes the corner eddy present in flows over backward facing steps. This undoubtedly has an effect on the reattachment length and the dynamics of the recirculation zone.

The slight Reynolds number effect is not seen in the profiles of lower-guidewall pressure coefficient,

$$C_p\,(x/L) = \frac{p\,(x/L) - p_i}{\frac{1}{2}\rho U_1^2} \tag{3.1}$$

plotted in Fig. 3.5, which is arguably a more robust measure of the reattachment length. These profiles collapse very well over the range of inlet velocities studied, with no visible Reynolds number effect, indicating that the reattachment length is independent of Reynolds number over the range studied. Comparing the lower-guidewall pressure profiles to those of Narayanan et al. (1974), measured with a fully turbulent boundary layer before separation, implies that the reattachment point is located at, or slightly downstream of, the probe location for these experiments. This profile also agrees reasonably well with data from Adams and Johnston (1988), Jaroch and Fernholz (1989), Kim et al. (1980), Ötugen (1991), Westphal and Johnston (1984), and Ruderich and Fernholz (1986). Although negative velocities were not directly measured at the probe location, the reattachment point is unsteady, so there could be many flow reversals at the probe location while the average total pressure is still larger than the static pressure.

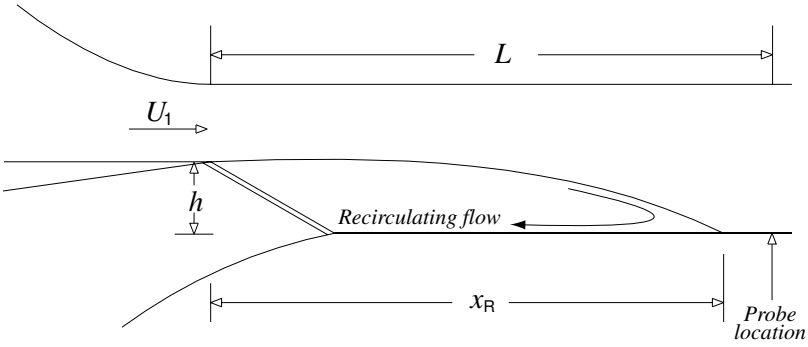

Figure 3.1: Cartoon of flow with solid ramp.

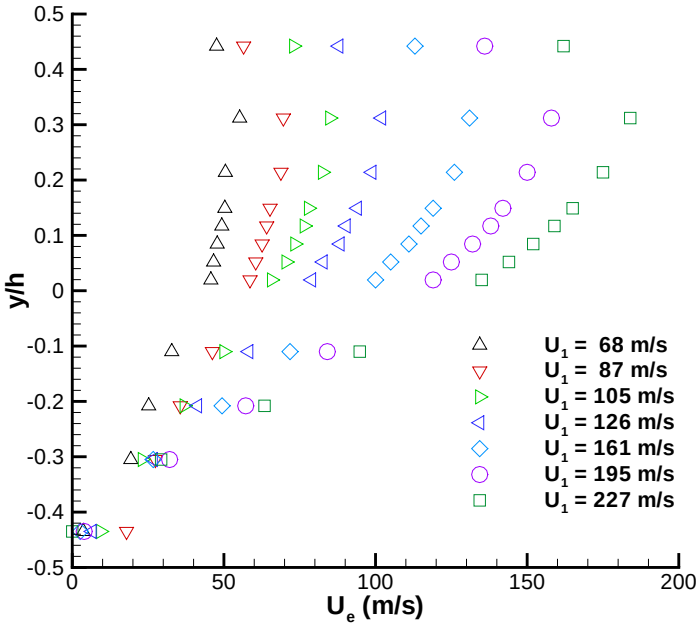

Figure 3.2: Exit velocity profile with no mass injection (solid ramp).

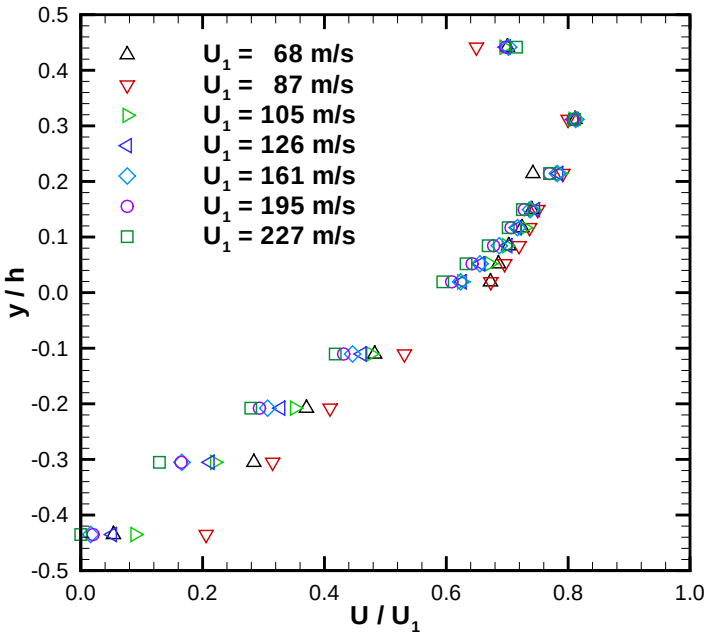

Figure 3.3: Normalized exit velocity profile with no mass injection (solid ramp).

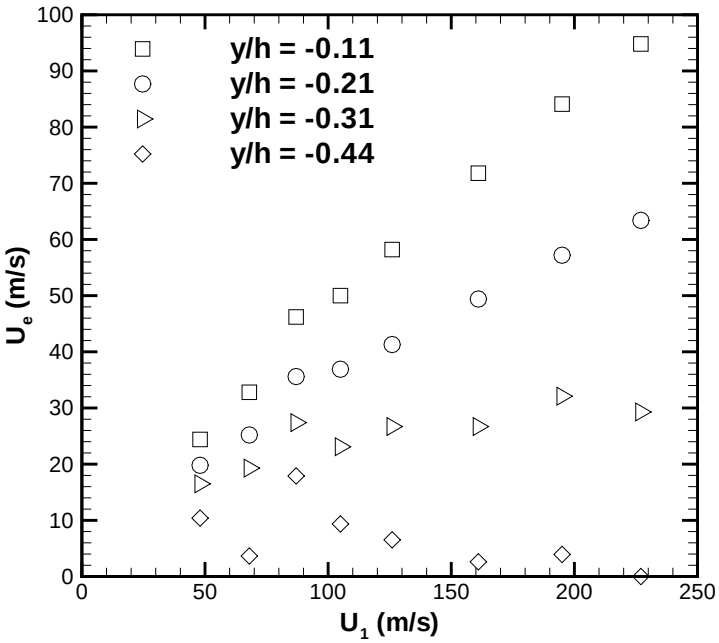

Figure 3.4: Exit velocity at four lowest probe locations.

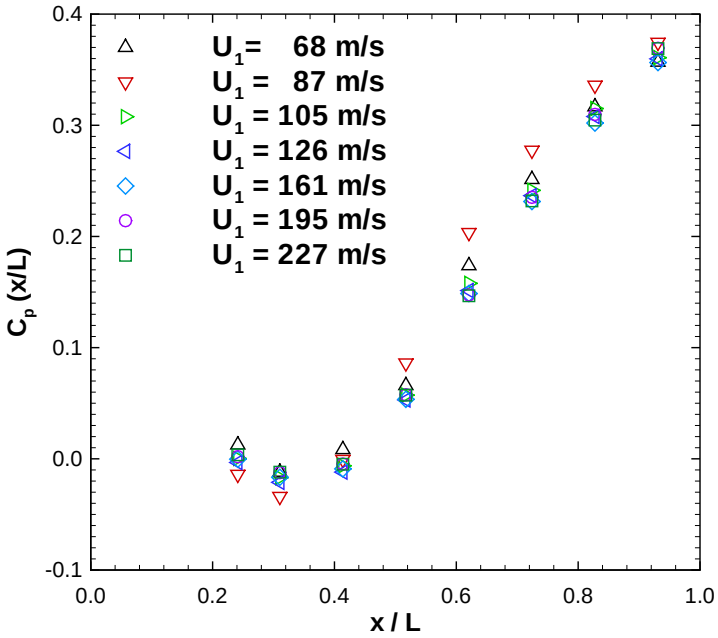

Figure 3.5: Lower-guidewall pressure coefficient with solid plate and no mass injection.

3.2 Flow With Mass Injection

Experiments were conducted to investigate the behaviour of the flow with variable mass injection through the perforated plate. With increasing mass injection, the recirculation zone is pushed further and further downstream. This manifests itself in the profiles of normalized exit velocity, and upper- and lower-guidewall pressure coefficient, as well as schlieren visualization.

Figure 3.6 plots the normalized exit velocity profile for $U_1 \approx 120\,\mathrm{m/s}$ over a range of injectant velocities, U_2, as shown in the legend. With mass injection, the flow in the upper part of the test section is accelerated while the flow in the lower part transitions to a re-entrant jet. As the reattachment point moves downstream, more of the probes are present inside the recirculation zone. While the velocity measurements in this region are not reliable from the pitot probe, as the total pressure measured is lower than the static pressure, the values were confirmed by integrating the profile and comparing to the total incoming mass flux from the upper and lower streams. For the highest level of mass injection studied, the backflow velocity measured at the lowest probe location is nearly 20% of the upper-stream inlet velocity.

Yang et al. (1994) conducted experiments with normal mass injection downstream of a backward-facing step with freestream velocities of 20 and 60 m/s. With increasing levels of mass injection, both the mean velocity and the maximum reverse velocity near the lower wall within the recirculation zone decreased.

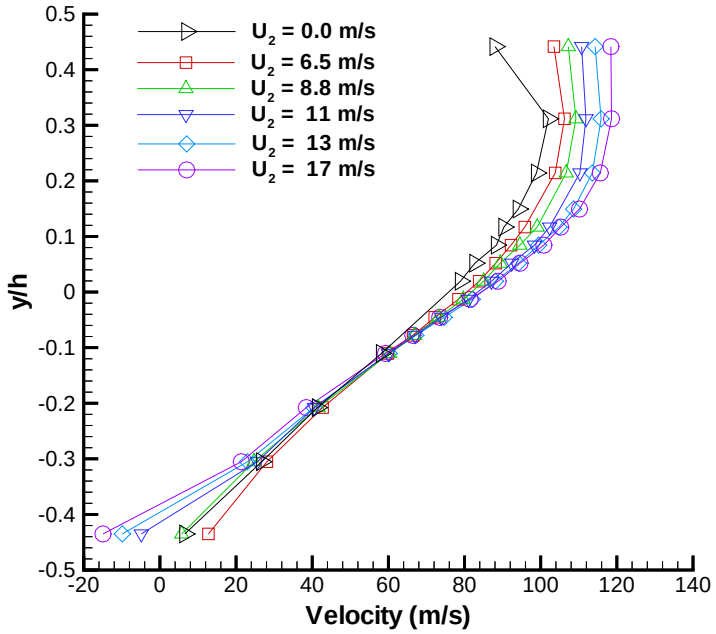

Figure 3.6: Exit velocity profile with variable mass injection. Upper stream: $U_1 \approx 120\,\mathrm{m/s}$ [N_2]. Lower stream: velocity as indicated in legend [66.66% Ar; 33.33% He].

Figure 3.7 plots the upper-guidewall pressure coefficient for the same levels of mass injection. Interestingly, the pressure minima at $x/L \sim 0.4$–0.5 in Fig. 3.7 indicate that the injected fluid acts as an aerodynamic nozzle on the freestream fluid, accelerating it over this range. In Fig. 3.8, a plot of the lower-guidewall pressure coefficient, the recirculation zone is seen as a region of near-uniform pressure, that is clearly pushed further downstream with increasing mass injection. Yang et al. (1994) also noted increased pressure recovery in the redevelopment region with increasing normal mass injection.

The movement of the reattachment zone further downstream as the mass injection level is increased was confirmed through schlieren visualization. Figure 3.9 shows a schlieren visualization of the flow with freestream velocity $\mathrm{U}_1 \approx 120\,\mathrm{m/s}$ and injectant velocity $\mathrm{U}_2 \approx 11\,\mathrm{m/s}$. Just downstream of the perforated ramp is a region of pure injected fluid. Further downstream is the recirculation zone where injected fluid mixes, at very reduced strain rates, with freestream fluid. With the same freestream velocity ($\mathrm{U}_1 \approx 120\,\mathrm{m/s}$) and an increased injectant velocity ($\mathrm{U}_2 \approx 25\,\mathrm{m/s}$), shown in Fig. 3.10, the recirculation zone has been blown downstream, and the flow is tending toward a classical free shear layer. Similar behaviour is observed for an upper-stream velocity of $U_1 \approx 68\,\mathrm{m/s}$ in Figs. 3.11 ($\mathrm{U}_2 \approx 7\,\mathrm{m/s}$) and 3.12 ($\mathrm{U}_2 \approx 12\,\mathrm{m/s}$).

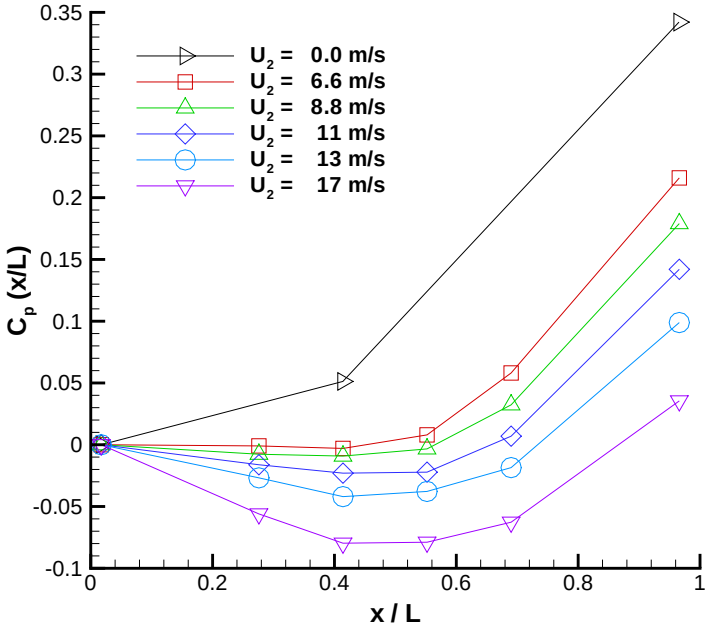

Figure 3.7: Upper-guidewall pressure coefficient with variable mass injection. Upper stream: $U_1 \approx 120\,\mathrm{m/s}$ [N_2]. Lower stream: velocity as indicated in legend [66.66% Ar; 33.33% He].

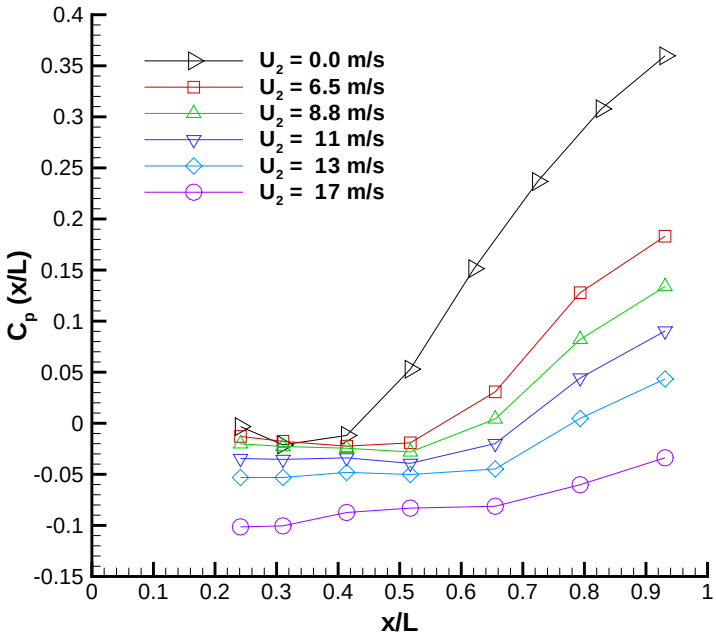

Figure 3.8: Lower-guidewall pressure coefficient with variable mass injection. Upper stream: $U_1 \approx 120\,\mathrm{m/s}$ [N_2]. Lower stream: velocity as indicated in legend [66.66% Ar; 33.33% He].

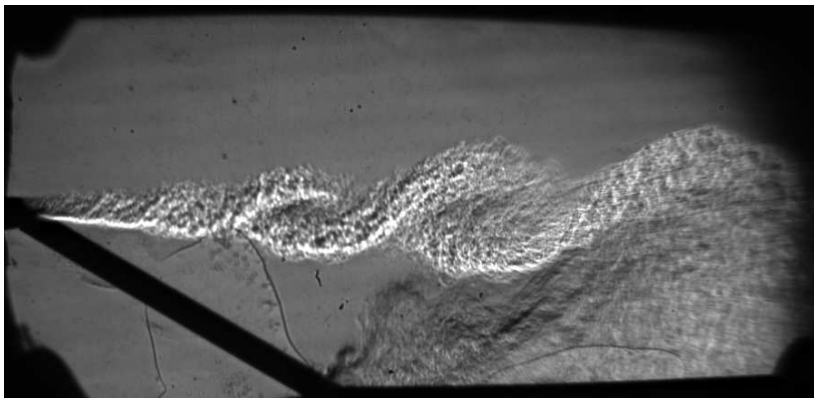

Figure 3.9: Schlieren visualization of non-reacting flow. Upper stream: $U_1 \approx 120\,\mathrm{m/s}$ [N_2]. Lower stream: $U_2 \approx 11\,\mathrm{m/s}$ [66.66% Ar; 33.33% He].

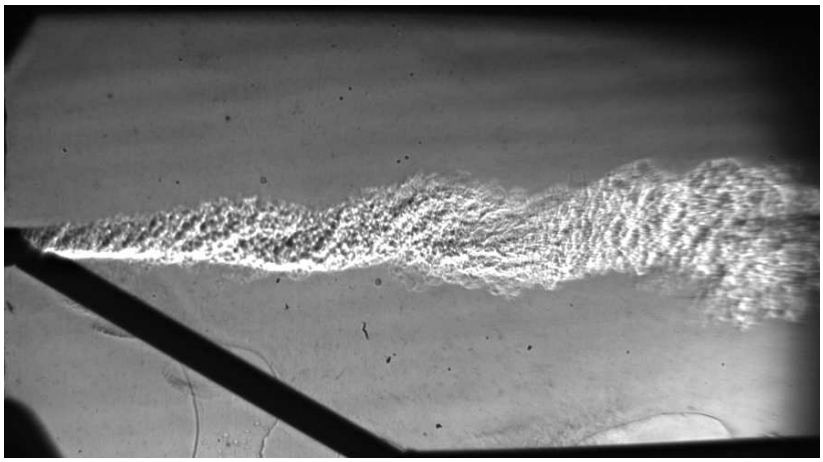

Figure 3.10: Schlieren visualization of non-reacting flow. Upper stream: $U_1 \approx 120\,\mathrm{m/s}$ [N_2]. Lower stream: $U_2 \approx 25\,\mathrm{m/s}$ [66.66% Ar; 33.33% He].

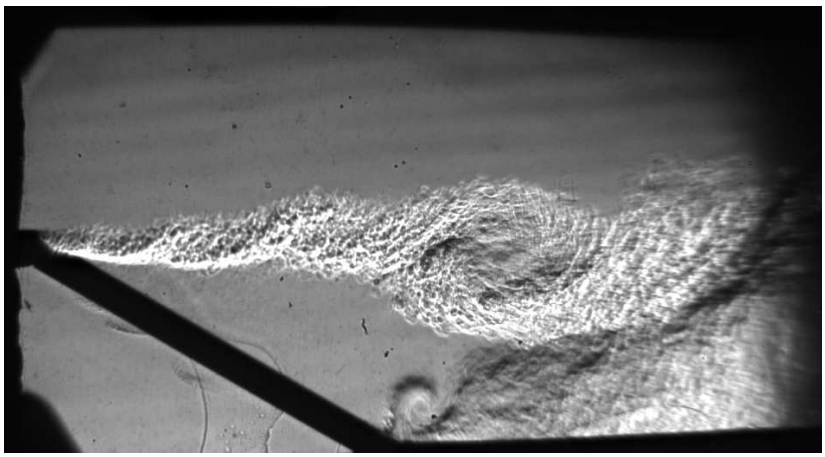

Figure 3.11: Schlieren visualization of non-reacting flow. Upper stream: $U_1 \approx 68\,\mathrm{m/s}$ [N_2]. Lower stream: $U_2 \approx 7\,\mathrm{m/s}$ [66.66% Ar; 33.33% He].

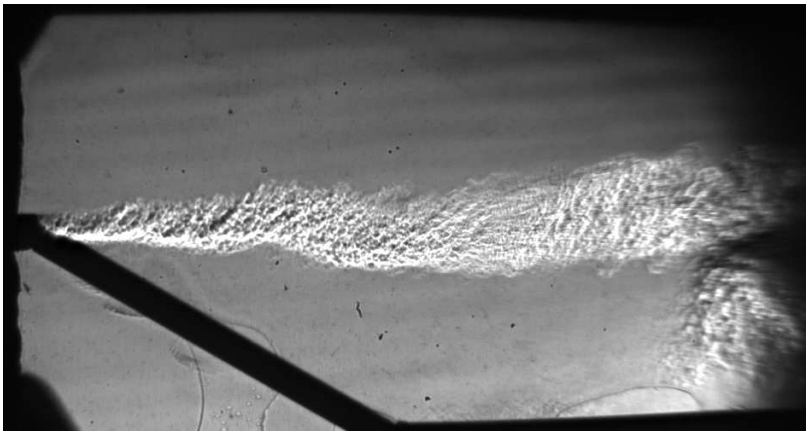

Figure 3.12: Schlieren visualization of non-reacting flow. Upper stream: $U_1 \approx 68\,\mathrm{m/s}$ [N_2]. Lower stream: $U_2 \approx 12\,\mathrm{m/s}$ [66.66% Ar; 33.33% He].

3.3 Pressure Coefficient Control

An important quantity in these flows is the overall pressure coefficient,

$$C_p = \frac{p_\mathrm{e} - p_\mathrm{i}}{\frac{1}{2}\rho_1 U_1^2} \tag{3.2}$$

where p_e and p_i are the (upper-guidewall) pressures at the test section exit and inlet, and U_1 is the upper-stream inlet velocity. Figure 3.13 plots the overall pressure coefficient as a function of the injection velocity ratio, U_2/U_1, for three different inlet velocities. The flow can be controlled from a fully stalled diffuser to a near-classical free shear layer, with negligible streamwise pressure gradient, by varying the injected mass flux. There is a slight increase in control authority as the inlet velocity, U_1, is increased. At higher inlet velocities, the injected mass flux ratio required to achieve the same overall pressure coefficient is lower.

A simple control-volume analysis was performed to put bounds on the performance of the flow. Assuming that the flow exits with a uniform velocity profile, $U = U_e$ over the entire height of the test section, the overall pressure coefficient with no mass injection is

$$C_p = 2\alpha\,(1 - \alpha) \tag{3.3}$$

where $\alpha = A_i/A_e$ is the ratio of inlet to exit area. In this geometry, $\alpha \simeq 0.52$, so $C_p\,(U_2 = 0) = 0.5$. Adding mass injection into this model yields a pressure coefficient of

$$C_p = 1/2 - \beta^2 - 2\beta \tag{3.4}$$

where $\beta = U_2/U_1$ is the injection velocity ratio. This model is plotted in Fig. 3.13 along with the

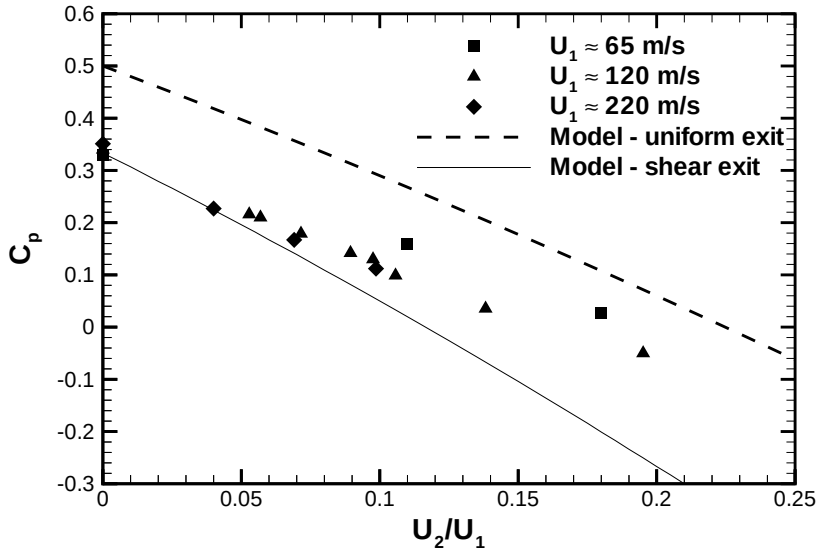

Figure 3.13: Overall pressure coefficient versus injection velocity ratio.

experimental data.

Another possibility is to model the exit velocity profile as a shear profile, which would seem to match the data more closely (*cf.* Figs. 3.3 and 3.6). With this model,

$$C_p = 1/3 - (5/3)\beta^2 - (8/3)\beta \tag{3.5}$$

which is also plotted in Fig. 3.13.

As can be seen in Fig. 3.13, the model with the uniform exit velocity profile overpredicts the data and the model with a shear profile, while it matches the data for $\beta = 0$, underpredicts for the range of β tested. These two models thus bound the performance of the diffuser flow. These models, however, do not take into account the variation in static pressure between the upper and lower guidewall, which increases with increasing mass injection.

3.4 Supersonic Flow

Experiments have also been conducted to investigate the behaviour of the flow in this geometry with a supersonic inflow. Figure 3.14 is a composite schlieren visualization of the flow with an inlet Mach number, $M_1 \sim 1.02$, from two separate experiments. Expanding slightly over the ramp, the flow initially accelerates to $M \sim 1.05$. As in the subsonic visualizations (Figs. 3.9–3.12), a pocket of

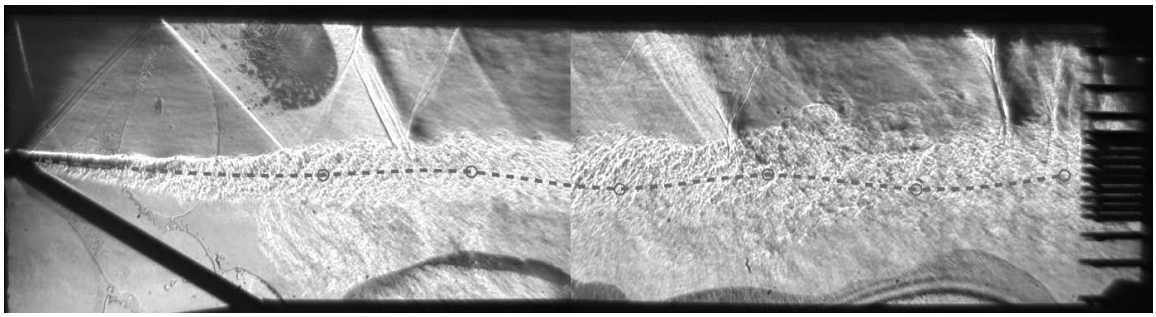

Figure 3.14: Composite schlieren visualization of supersonic flow with ramp injection, from two separate experiments. Upper stream: Mach number $M_1 \sim 1.02$ [N_2]. Lower stream: $U_2 \approx 15\,\mathrm{m/s}$ [66.66% Ar; 33.33% He]. Circles and dotted line represent freestream area ratio, A/A_*, calculated from upper-guidewall pressure data.

pure injected fluid is visible just downstream of the ramp. The recirculation zone extends further downstream, all the way to the test section exit. For this flow, measured upper-guidewall static pressures are in accord with those estimated from Mach numbers based on the flow-visualization data. Importantly, freestream area ratio, $A\left(x\right)/A_*$, estimated from upper-guidewall pressure data, agrees well with the visual shear-layer thickness, assuming negligible entropy production, *i.e.*, negligible total-pressure losses. The recirculation zone and low total-pressure losses in supersonic flow make this geometry promising as a basis for a supersonic combustor.

Chapter 4

Reacting Flow

As mentioned in Chapter 2, the S^3L facility is designed to handle fast-kinetic reactants, specifically H_2 and NO in the upper stream, and F_2 in the lower stream. By varying the concentrations of these reactants it is possible to measure molecular mixing between the two streams with the "flip" experiment (Mungal and Dimotakis, 1984; Koochesfahani and Dimotakis, 1986), and to investigate the effects of variable heat release on the flow-field. In this investigation, both of these capabilities were utilized.

4.1 Flip Experiment

The "flip" experiment is so-called as it involves computing statistics from two experiments; one is performed with the high-speed stream rich in reactants, and the other where the compositions have been "flipped" and the lower-stream is rich in reactants. An important quantity in this experiment is the stoichiometric mixture ratio, ϕ, defined as the number of moles of high-speed fluid needed to fully consume one mole of low-speed fluid,

$$\phi = \frac{X_2/X_1}{(X_2/X_1)_{\mathrm{st}}} \tag{4.1}$$

where X_1 and X_2 are the reactant concentrations in the upper and lower streams, and the subscript "st" denotes a stoichiometric mixture. For example, an experiment conducted at $\phi = 8$ denotes that 8 moles of upper-stream fluid must mix with 1 mole of lower-stream fluid in order for all reactants to be consumed. For the reaction system used in these experiments, with main reaction $H_2 + F_2 \rightarrow 2\,HF$ and chain branching reaction $NO + F_2 \rightarrow NOF + F$,

$$\phi = \frac{[F_2]}{[H_2] + \frac{[NO]}{2}} \tag{4.2}$$

The mixture mole fraction, ξ, is defined as the concentration of upper-stream fluid, $\xi = n_1/(n_1 + n_2)$,

where n_1 and n_2 represent the number of moles of upper- and lower-stream fluid, respectively. Thus, the reactants will be completely consumed at a stoichiometric mixture mole fraction

$$\xi_\phi = \frac{\phi}{\phi + 1} \tag{4.3}$$

The relative amount of product that can be formed at a particular mixture fraction is called the normalized product function, $\theta(\xi; \xi_0)$. Assuming complete consumption of the lean reactant, this is computed as

$$\theta(\xi; \xi_\phi) = \begin{cases} \frac{\xi}{\xi_\phi} & \text{for } 0 \le \xi \le \xi_\phi \\ \frac{1-\xi}{1-\xi_\phi} & \text{for } \xi_\phi \le \xi \le 1 \end{cases} \tag{4.4}$$

and plotted in Fig. 4.1 for $\phi = 8$ and $\phi = 1/8$, along with a hypothetical mixed fluid probability density function (pdf). As expected, the normalized product function reaches a value of one for a stoichiometric mixture fraction, where by definition all reactants would be consumed. The pdf is also a function of the vertical location, y — the sketch shown would correspond to a vertical location somewhere inside the region of mixed fluid. For a shear layer in an infinite domain, as $y \to -\infty$ the pdf becomes a delta function of pure lower-stream fluid at $\xi = 0$, and as $y \to +\infty$ the pdf becomes a delta function of pure upper-stream fluid at $\xi = 1$.

For a given experiment, the measured temperature rise profile, normalized by the adiabatic flame temperature rise, ΔT_f, is equal to the integral of the product of the mixed fluid pdf and the normalized product function (Dimotakis, 1991),

$$\int_0^1 \theta(\xi; \xi_\phi)\, p(\xi, y)\, \mathrm{d}\xi = \frac{\Delta T(y; \phi)}{\Delta T_\mathrm{f}} \tag{4.5}$$

Again, if all fluid were at a mixture fraction ξ_ϕ, where the normalized product function is equal to 1, the pdf would be a delta function at that composition, and the temperature rise would be everywhere equal to the adiabatic flame temperature rise, ΔT_f.

By performing experiments at high and low values of ϕ, it is possible to estimate the probability of mixed fluid as a function of y,

$$P_\mathrm{m}(y) \equiv \int_\epsilon^{1-\epsilon} p(\xi, y)\, \mathrm{d}\xi \tag{4.6}$$

ignoring the contribution from the unmixed fluid at the edges of the pdf. The sum of the two normalized product functions at high and low ϕ, shown in Fig. 4.1 for $\phi = 1/8$ and $\phi = 8$, reaches a constant value of $1/(1 - \xi_0)$ between ξ_0 and $1 - \xi_0$, where $\xi_0 = 1/9$ in this case. Thus, $P_\mathrm{m}(y)$ is

estimated from the measured temperature rise for the two cases,

$$P_{\mathrm{m}}(y) \approx (1-\xi_0)\int_0^1 \left[\theta(\xi;\phi=1/8)+\theta(\xi;\phi=8)\right] p(\xi,y)\,\mathrm{d}\xi \tag{4.7}$$

$$\approx (1-\xi_0)\left[\left.\frac{\Delta T(y)}{\Delta T_{\mathrm{f}}}\right|_{\phi=1/8}+\left.\frac{\Delta T(y)}{\Delta T_{\mathrm{f}}}\right|_{\phi=8}\right] \tag{4.8}$$

Ignoring curvature at the edges of the pdf sets the limits of integration of Eqn. 4.6 as $\epsilon \simeq \xi_0/2$.

For a free shear layer, the mixing-region thickness, δ_{T}, is calculated as the span between the two points where the normalized temperature profile reaches 1% of its maximum value. In this geometry, since the mixing region extends all the way down to the lower guidewall, δ_{T} is calculated as the distance from the lower guidewall to the point where the temperature-rise profile reaches 1% of its maximum value. The product thickness, δ_{P}, is defined as,

$$\delta_{\mathrm{P}} \equiv \int_{-\infty}^{\infty} \frac{\Delta T(y)}{\Delta T_{\mathrm{f}}}\,\mathrm{d}y \tag{4.9}$$

which represents the thickness of an equivalent mixing region that has risen uniformly to the adiabatic flame temperature.

The average composition in the mixed fluid,

$$\overline{\xi}_{\mathrm{m}} = \frac{\displaystyle\int_{-\infty}^{\infty}\int_{\epsilon}^{1-\epsilon} \xi p(\xi,y)\,\mathrm{d}\xi\,\mathrm{d}y}{\displaystyle\int_{-\infty}^{\infty}\int_{\epsilon}^{1-\epsilon} p(\xi,y)\,\mathrm{d}\xi\,\mathrm{d}y} \tag{4.10}$$

can be calculated as follows. From Eqn. 4.4, for $\xi_\phi = 1-\xi_0$ ($\phi = 8$ in these experiments), $\xi = \xi_\phi\,\theta(\xi;\xi_\phi) = (1-\xi_0)\,\theta(\xi;1-\xi_0)$. Thus,

$$\int_{-\infty}^{\infty}\int_{\epsilon}^{1-\epsilon} \xi p(\xi,y)\,\mathrm{d}\xi\,\mathrm{d}y = (1-\xi_0)\int_{-\infty}^{\infty}\int_{\epsilon}^{1-\epsilon} \theta(\xi;1-\xi_0)\,p(\xi,y)\,\mathrm{d}\xi\,\mathrm{d}y \tag{4.11}$$

From Eqns. 4.5 and 4.9, this integral is equal to $(1-\xi_0)\,\delta_{\mathrm{P}}(1-\xi_0)$, where $\delta_{\mathrm{P}}(1-\xi_0)$ is the product thickness for the $\phi = 8$ experiment.

From Eqns. 4.6, 4.8, and 4.9, the integral in the denominator becomes

$$\int_{-\infty}^{\infty}\int_{\epsilon}^{1-\epsilon} p(\xi,y)\,\mathrm{d}\xi\,\mathrm{d}y = \int_{-\infty}^{\infty} P_{\mathrm{m}}(y)\,\mathrm{d}y = (1-\xi_0)\left[\delta_{\mathrm{P}}(\xi_0)+\delta_{\mathrm{P}}(1-\xi_0)\right] \tag{4.12}$$

where $\delta_{\mathrm{P}}(\xi_0)$ is the product thickness for the $\phi = 1/8$ experiment, and $\delta_{\mathrm{P}}(1-\xi_0)$ is the product thickness for the $\phi = 8$ experiment.

Thus,

$$\overline{\xi}_{\mathrm{m}} = \frac{\delta_{\mathrm{P}}(1-\xi_0)}{\delta_{\mathrm{P}}(\xi_0)+\delta_{\mathrm{P}}(1-\xi_0)} \tag{4.13}$$

			Upper Stream						Lower Stream				
	ϕ	ΔT_f	U_1	H_2	NO	N_2	He	Ar	U_2	F_2	N_2	He	Ar
(a)	1/8	94 K	120 m/s	4.44	0.24	75.76	11.56	8.00	11 m/s	0.57	76.00	16.00	5.68
	8	50 K	120 m/s	0.27	0.04	75.96	15.73	8.00	11 m/s	2.32	76.00	16.00	5.68
(b)	1/8	200 K	120 m/s	8.88	0.48	75.52	7.12	8.00	11 m/s	1.14	76.00	16.00	6.86
	8	102 K	120 m/s	0.55	0.08	75.92	15.45	8.00	11 m/s	4.72	76.00	16.00	3.28

Table 4.1: Speeds and compositions (mole percent) used for flip experiments. (a) low heat release; (b) higher heat release.

A mixing region entraining upper- and lower-stream fluid at a ratio E, which is being homogenized by the action of turbulence, will tend towards an average composition (Dimotakis, 1986, 1991),

$$\xi_E = \frac{E}{E+1} \tag{4.14}$$

Solving for E leads to a definition of the entrainment ratio for the mixing region,

$$E_n = \frac{\overline{\xi}_m}{1-\overline{\xi}_m} = \frac{\delta_P\,(1-\xi_0)}{\delta_P\,(\xi_0)} \tag{4.15}$$

The total mixed fluid fraction, δ_m/δ_T, is the integral of the spatial mixed fluid probability, $P_m\,(y)$, scaled by the mixing region thickness, δ_T, and can be estimated using Eqns. 4.6 and 4.8,

$$\frac{\delta_m}{\delta_T} = \int_{-\infty}^{\infty}\int_{\epsilon}^{1-\epsilon} p\,(\xi,\hat{y})\,\mathrm{d}\xi\;\mathrm{d}\hat{y} = \int_{-\infty}^{\infty} P_m\,(\hat{y})\,\mathrm{d}\hat{y} = (1-\xi_0)\left[\frac{\delta_P}{\delta_T}\,(\xi_0) + \frac{\delta_P}{\delta_T}\,(1-\xi_0)\right] \tag{4.16}$$

where $\hat{y} = y/\delta_T$.

Experiments have been performed at $\phi = 1/8$ and $\phi = 8$, with velocities $U_1 \approx 120\,m/s$ and $U_2 \approx 11\,m/s$. Two cases have been studied: case (a) at low heat release with a maximum temperature rise of approximately 30 K and case (b) at higher heat release with a maximum temperature rise of approximately 80 K. It was necessary to tailor the adiabatic flame temperatures for each case in order that the exit velocity profiles match for the high and low ϕ experiments. Otherwise, it would not be possible to compute statistics from the two experiments since there is an implicit assumption that the flow is essentially unchanged for high and low ϕ. The compositions used are listed in Table 4.1.

Temperature profiles for the two cases are shown in Fig. 4.2, along with curve fits using the equation,

$$\Delta T = \exp\left(a_0 + a_1\,(y_*) + a_2(y_*)^2 + a_3(y_*)^3 + a_4(y_*)^4 + a_5(y_*)^5\right) \tag{4.17}$$

where $y_* = y/h$ (h is the test section height). All statistics described below were calculated from the curve fits. Fig. 4.2 also illustrates the characteristic shift of the peak temperature-rise location towards the stream with the lean reactant.

Figure 4.3 shows the normalized temperature-rise profiles for each case. It is seen that the normalized temperature rise is nearly twice as large for the experiments with the lower stream rich in reactants. This illustrates that the mixing zone in this geometry is biased towards upper-stream fluid much more than a classical shear layer, where this difference is not nearly as large.

Using the shear-layer entrainment model based on the large-scale structure spacing (Dimotakis, 1986), the molar entrainment ratio of a classical, density-matched shear layer is

$$E_{\mathrm{n}} = \frac{U_1 - U_{\mathrm{c}}}{U_{\mathrm{c}} - U_2} \left(1 + 0.68 \left(\frac{1-r}{1+r}\right)\right) \tag{4.18}$$

where $r = U_2/U_1$ is the velocity ratio and U_{c} is the convection velocity of the large-scale structures. For a density-matched shear layer, $U_{\mathrm{c}} = (U_1 + U_2)/2$. A classical shear layer with a velocity ratio as in these experiments would have a molar entrainment ratio, $E_{\mathrm{n}} = 1.57$. An entrainment ratio of 2.37 for case (a) and 1.87 for case (b) was measured with the flip experiments, from Eqn. 4.15 — an increase of 50% and 20%, respectively, over a classical free shear layer. Strictly speaking, this model is not applicable to this geometry as the entrainment mechanism is modified due to the recirculation zone, but this does still illustrate the increased amount of upper-stream fluid that is being entrained into the mixing region.

The flip experiments yielded total mixed fluid fractions of $\delta_{\mathrm{m}}/\delta_{\mathrm{T}} = 0.64$ for case (a) and 0.71 for case (b). These represent increases of 31% and 45% over the value of $\delta_{\mathrm{m}}/\delta = 0.49$ quoted in Dimotakis (1991) for classical free shear layers. The mixed fluid fraction is initially increasing with increasing heat release.

An important quantity in this flow, and in flows in supersonic combustors, is the flux of mixed fluid exiting the test section. Figure 4.4 plots the normalized exit velocity, the probability of mixed fluid, and their product, called the mixed fluid flux, for the two cases studied. In the recirculation zone the probability of mixed fluid reaches nearly one, indicating the large potential of this region for mixing and flameholding in supersonic combustors. Integrating the profiles of mixed fluid flux and normalized exit velocity,

$$\frac{\displaystyle\int_{-0.5}^{0.5} P_{\mathrm{m}}(y_*)\,\frac{U(y_*)}{U_1}\,\mathrm{d}y_*}{\displaystyle\int_{-0.5}^{0.5} \frac{U(y_*)}{U_1}\,\mathrm{d}y_*} \tag{4.19}$$

yields a volume fraction of mixed fluid exiting the test section of 0.32 for case (a) and 0.37 for case (b). As with the mixed fluid fraction, $\delta_{\mathrm{m}}/\delta_{\mathrm{T}}$, this is increasing with increasing heat release. A discussion of the effects of heat release follows in Section 4.2.

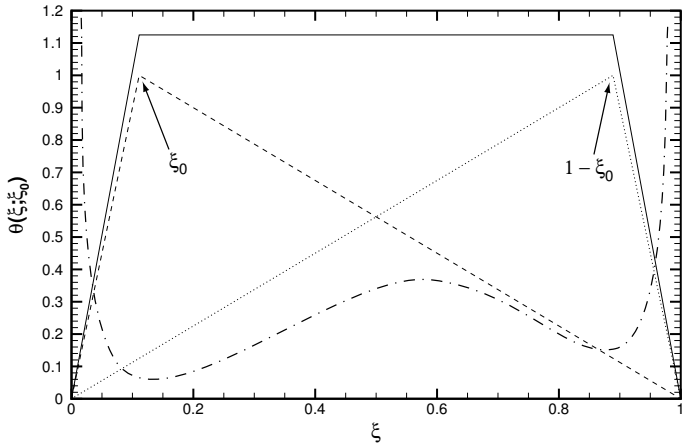

Figure 4.1: Normalized chemical product function (Equation 4.4). $\phi = 1/8$ (dashed line), $\phi = 8$ (dotted line), and the sum (solid line). Mixture fraction probability density function (pdf) sketched for reference (dot-dashed line). Figure adapted from Dimotakis (1991).

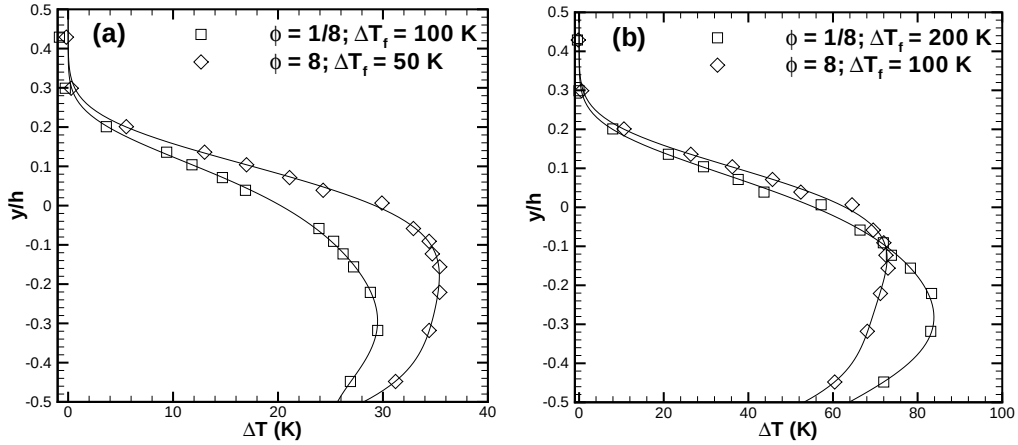

Figure 4.2: Temperature-rise profiles for flip experiment. (a) low heat-release case, (b) higher heat-release case.

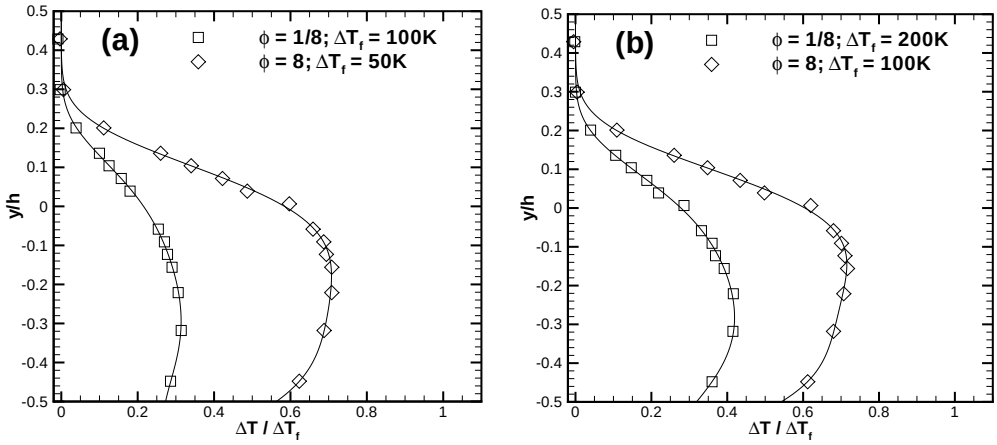

Figure 4.3: Normalized temperature-rise profiles for flip experiment: (a) low heat-release, (b) higher heat-release.

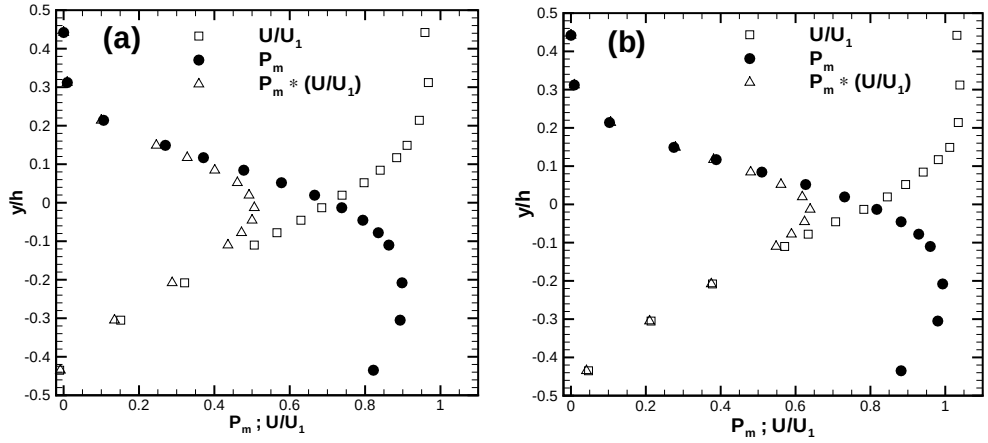

Figure 4.4: Probability of mixed fluid, normalized exit velocity, and mixed fluid flux profiles for flip experiment: (a) low heat-release, (b) higher heat-release.

4.2 Heat Release Effects

A series of experiments was performed to measure the behaviour of the flow with varying levels of heat release. These experiments were performed at $\phi \approx 1$ with increasing concentrations of H_2 and F_2. The compositions used are listed in Table 4.2.

Figure 4.5 plots the temperature rise profiles for this series of experiments, and Fig. 4.6 plots the normalized temperature rise profiles. Figure 4.7 plots the peak and integral of the normalized temperature rise. The integral is equivalent to the product thickness, δ_P from Equation 4.9, scaled by the test-section height, h.

$$\frac{\delta_P}{h} = \int_{-0.5}^{0.5} \frac{\Delta T\,(y_*)}{\Delta T_f} \mathrm{d}y_* \tag{4.20}$$

Similar to the results of Section 4.1, the level of mixing initially increases with heat release until a concentration of approximately 2–4% ($\Delta T_f \sim 200$–$300\,\mathrm{K}$) at which point the level of mixing begins to decrease. As the heat release is further increased, the entrainment requirements of the shear layer decrease, and the recirculation zone is pushed further and further downstream. The mixing benefit at the measuring station thus decreases.

This was confirmed through the schlieren visualizations, shown in Figs. 4.8–4.11. The flow in Fig. 4.8 is very similar to the non-reacting flow in Fig. 3.9. In this case, the temperature rise from the chemical reaction is acting as a passive scalar with little effect on the overall flowfield. In Figs. 4.9 to 4.11, increasing levels of heat release have an effect on the flowfield — the recirculation zone is blown further and further downstream, and the flow is becoming more like a classical shear layer.

Figure 4.12 plots the exit velocity profiles for inert mass injection at the same velocity ratio, and for mass injection with variable heat release. Comparing this plot to that for inert flow with increasing mass injection (Fig. 3.6), it is seen that with heat release the flow in the entire test section is accelerated, whereas with inert mass injection the upper portion of the test section is accelerated while the lower portion transitions to a re-entrant jet.

Figure 4.13 plots the upper-guidewall pressure coefficient for flow with variable heat release. As was seen in Fig. 3.7 for inert mass injection, the pressure minima at $x/L \sim 0.4$–0.5 indicate that the injected fluid acts as an aerodynamic nozzle on the freestream fluid, accelerating it over this range. In this case, with constant mass injection, it is the dilatation from the chemical reaction that is accelerating the flow. In Fig. 4.14, a plot of the lower-guidewall pressure coefficient, the recirculation zone is seen as a region of near-uniform pressure that is clearly pushed further downstream with increasing heat release, as happens with increasing inert mass injection (Fig. 3.8). From these plots, it is seen that the dilatation from the chemical reaction at a fixed mass injection ratio has a similar effect on the flow-field as increasing inert mass injection does.

Fig 4.15 plots the overall pressure coefficient, including data from experiments with reacting flow. Additional control on the flowfield is possible with the addition of heat release. It is seen that, at

			Upper Stream				Lower Stream		
	ϕ	ΔT_f	U_1	$\%H_2$	$\%NO$	$\%N_2$	U_2	$\%F_2$	$\%N_2$
(a)	0.89	94 K	120 m/s	1.00	0.25	98.75	11 m/s	1.00	99.00
(b)	0.94	186 K	120 m/s	2.00	0.25	97.75	11 m/s	2.00	98.00
(c)	0.97	368 K	120 m/s	4.00	0.25	95.75	11 m/s	4.00	96.00
(d)	0.98	544 K	120 m/s	6.00	0.25	93.75	11 m/s	6.00	94.00

Table 4.2: Speeds and compositions (mole percent) used for heat-release study.

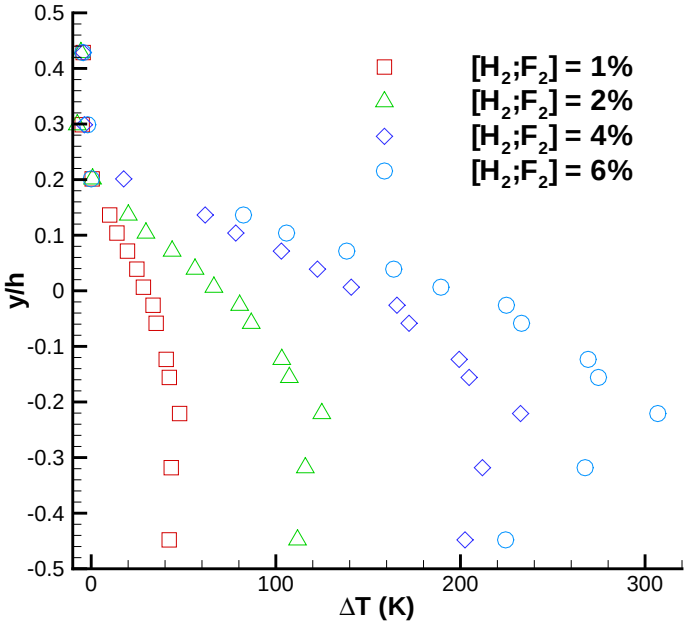

Figure 4.5: Temperature-rise profiles for increasing levels of heat release. $U_1 \approx 120\,\mathrm{m/s}$; $U_2 \approx 11\,\mathrm{m/s}$.

the highest heat release studied, mass injection requirements are lowered by nearly a factor of two relative to non-reacting flow. Thus, with reacting flow it is only necessary to inject half as much mass to achieve the same overall pressure coefficient.

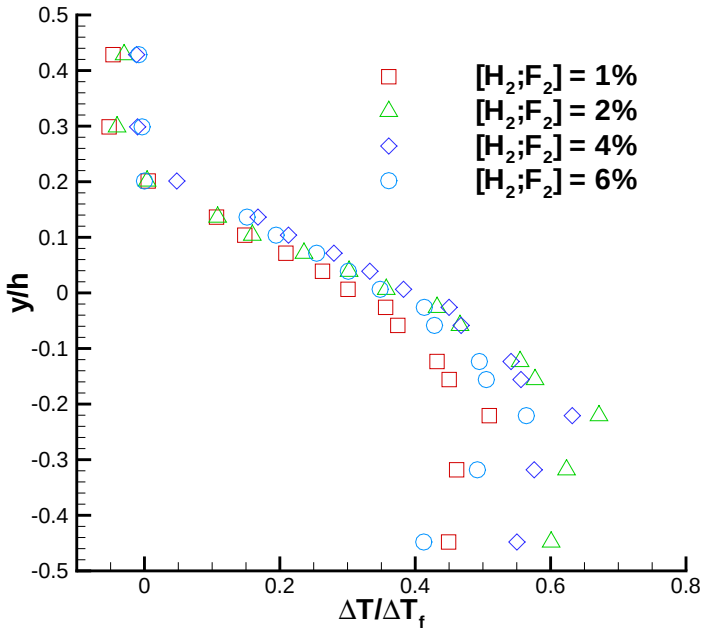

Figure 4.6: Normalized temperature-rise profiles for increasing levels of heat release. $U_1 \approx 120\,\mathrm{m/s}$; $U_2 \approx 11\,\mathrm{m/s}$.

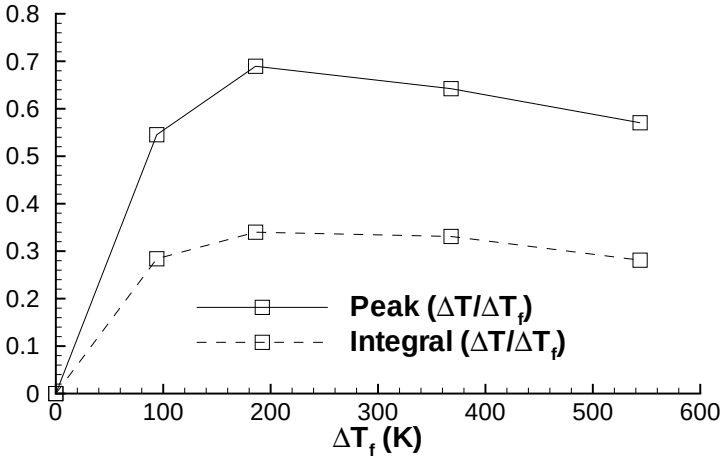

Figure 4.7: Peak and integral of normalized temperature rise profile.

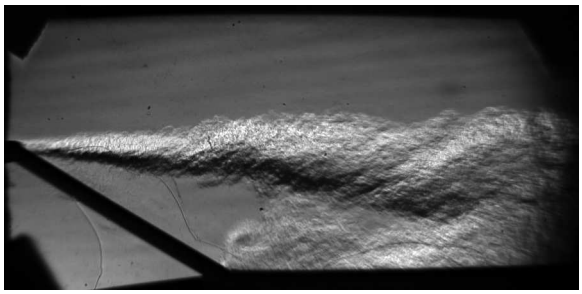

Figure 4.8: Schlieren visualization of reacting flow, case (a) from Table 4.2. Upper stream: $U_1 \approx 120\,\mathrm{m/s}$ [1.0% H_2; 0.25% NO; 98.75% N_2]. Lower stream: $U_2 \approx 11\,\mathrm{m/s}$ [1.0% F_2; 99.0% N_2].

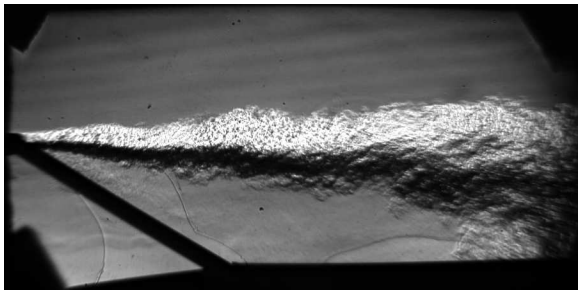

Figure 4.9: Schlieren visualization of reacting flow, case (b) from Table 4.2. Upper stream: $U_1 \approx 120\,\mathrm{m/s}$ [2.0% H_2; 0.25% NO; 97.75% N_2]. Lower stream: $U_2 \approx 11\,\mathrm{m/s}$ [2.0% F_2; 98.0% N_2].

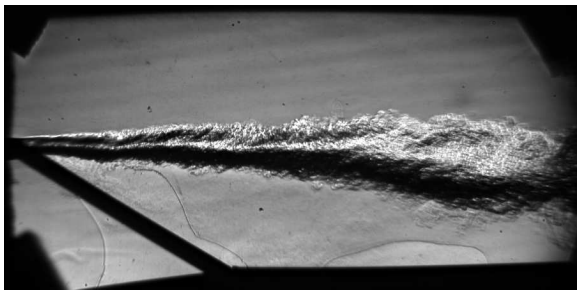

Figure 4.10: Schlieren visualization of reacting flow, case (c) from Table 4.2. Upper stream: $U_1 \approx 120\,\mathrm{m/s}$ [4.0% H_2; 0.25% NO; 95.75% N_2]. Lower stream: $U_2 \approx 11\,\mathrm{m/s}$ [4.0% F_2; 96.0% N_2].

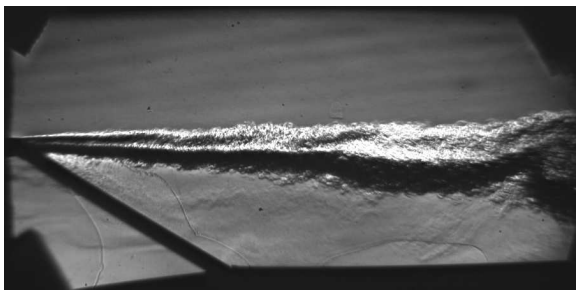

Figure 4.11: Schlieren visualization of reacting flow, case (d) from Table 4.2. Upper stream: $U_1 \approx 120\,\mathrm{m/s}$ [6.0% H_2; 0.25% NO; 93.75% N_2]. Lower stream: $U_2 \approx 11\,\mathrm{m/s}$ [6.0% F_2; 94.0% N_2].

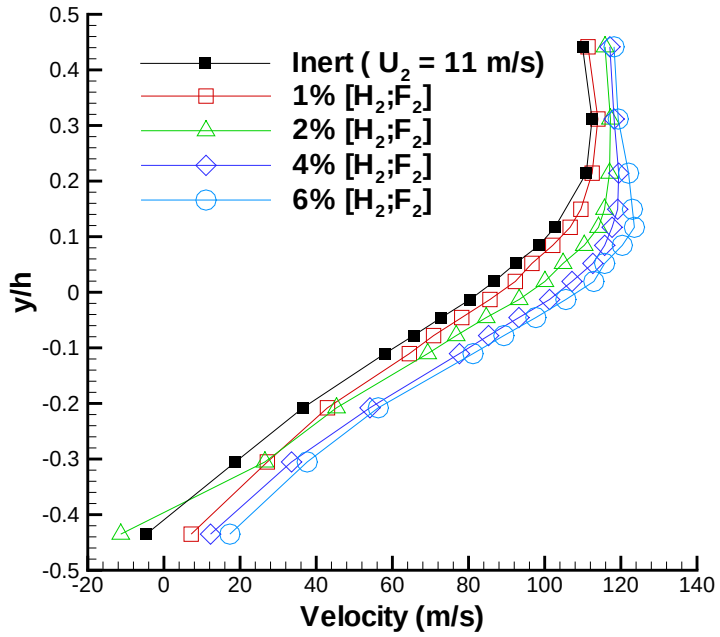

Figure 4.12: Exit velocity profiles for reacting flow. $U_1 \approx 120\,\mathrm{m/s}$; $U_2 \approx 11\,\mathrm{m/s}$.

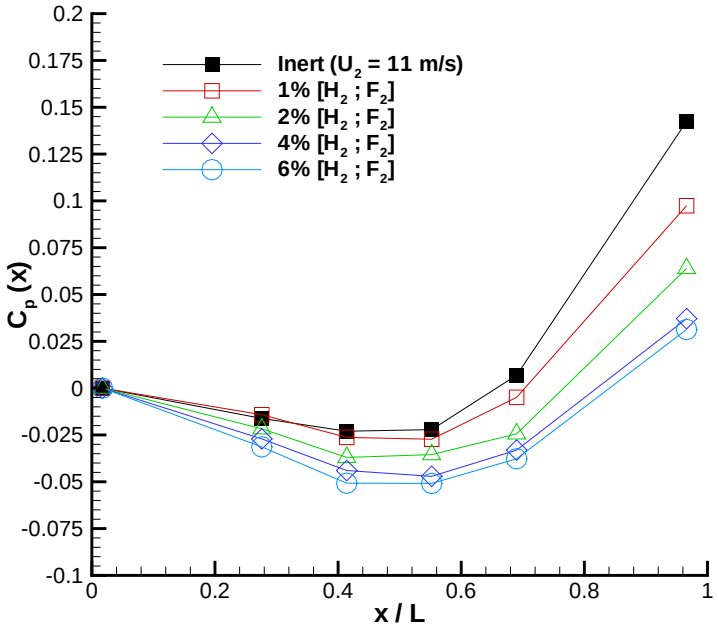

Figure 4.13: Upper-guidewall pressure coefficient. $U_1 \approx 120\,\mathrm{m/s}$; $U_2 \approx 11\,\mathrm{m/s}$.

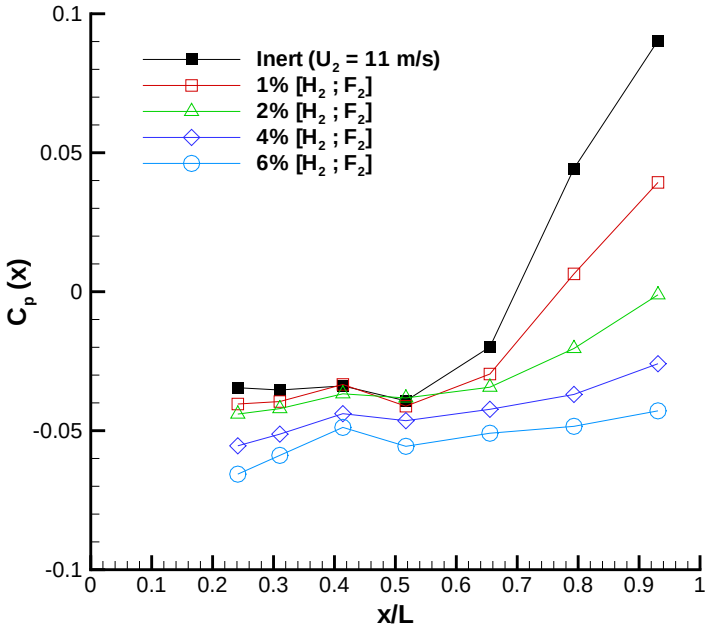

Figure 4.14: Lower-guidewall pressure coefficient. $U_1 \approx 120\,\mathrm{m/s}$; $U_2 \approx 11\,\mathrm{m/s}$.

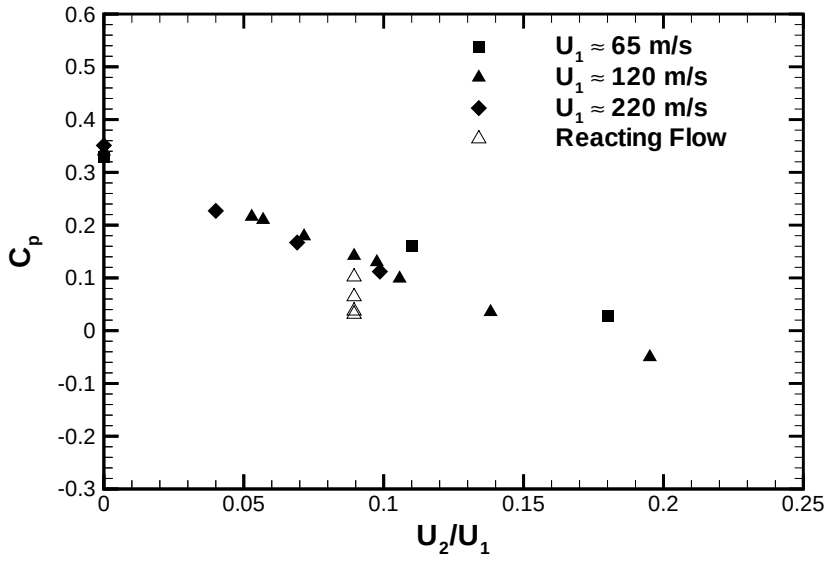

Figure 4.15: Overall pressure coefficient for reacting and non-reacting flow. Points for reacting flow correspond to $U_1 \approx 120\,\mathrm{m/s}$ and $U_2 \approx 11\,\mathrm{m/s}$, with H_2 and F_2 concentrations, from top to bottom, of 1, 2, 4 and 6%.

Chapter 5

Conclusions

The flow in a geometry with many potential benefits for supersonic mixing and combustion with low total pressure losses has been investigated. In a subsonic diffuser configuration with no mass injection, the exit velocity and guidewall pressure profiles collapse over a large range of inlet Reynolds numbers. Exit velocity profiles seem to indicate that the reattachment length increases slightly with increasing Reynolds number, which is not in accord with other published data. Lower-guidewall pressure measurements, however, do not exhibit this decrease, and collapse well over the entire Reynolds number range studied.

Significant control of exit velocity and guidewall pressure profiles is possible via injection through a perforated ramp. The control authority increases with increasing inlet Reynolds number. For higher inlet Reynolds numbers, the mass injection ratio required to achieve the same overall pressure coefficient is lower.

In supersonic flow with mass injection, the freestream area ratio calculated from the upper-guidewall pressure data agrees well with the visual shear layer thickness, indicating the low total-pressure losses present in the device, and illustrating its potential as a basis for a supersonic combustor.

Measurements from a fast chemical reaction indicate that a much higher fraction of fluid is mixed on a molecular scale in this geometry, versus a classical free shear layer. Mixing initially increases with increasing heat release but then begins to drop off beyond an adiabatic flame temperature rise $\Delta T_{\mathrm{f}} \sim 200\,\mathrm{K}$. Heat release from such a reaction also provides an additional level of control on the flowfield. At the highest heat release studied, it is only necessary to inject half as much mass to achieve the same control of the overall pressure coefficient.

References

Adams, E. W. and Johnston, J. P., 1988. Effects of the separating shear layer on the reattachment flow structure Part 1: Pressure and turbulence quantities. *Exp. Fluids*, 6:400–408.

Ben-Yakar, A. and Hanson, R. K., 2001. Cavity flame-holders for ignition and flame stabilization in scramjets: an overview. *Journal of Propulsion and Power*, 17(4):869–877.

Bradshaw, P. and Wong, F. Y. F., 1972. The reattachment and relaxation of a turbulent shear layer. *J. Fluid Mech.*, 52:113–135.

Dimotakis, P. E., 1986. Two-dimensional shear-layer entrainment. *AIAA Journal*, 24:1791–1796.

Dimotakis, P. E., 1991. Turbulent free shear layer mixing and dynamics. In *High-Speed Flight Propulsion Systems*, Progress in Astronautics and Aeronautics, chapter 5. AIAA.

Eaton, J. K. and Johnston, J. P., 1981. A review of research on subsonic turbulent flow reattachment. *AIAA Journal*, 19(9):1093–1100.

Gruber, M., Baurle, R., Mathur, T., and Hsu, K.-Y., 2001. Fundamental studies of cavity-based flameholder concepts for supersonic combustors. *Journal of Propulsion and Power*, 17(1): 146–153.

Hall, J. L., 1991. *An experimental investigation of structure, mixing and combustion in compressible turbulent shear layers.* California Institute of Technology, Ph.D. thesis.

Hall, J. L. and Dimotakis, P. E. Design overview of the supersonic hydrogen-fluorine facility (v4.0). Technical report, GALCIT, August 1989.

Jaroch, M. P. and Fernholz, H.-H., 1989. The three-dimensional character of a nominally two-dimensional separated turbulent shear flow. *J. Fluid Mech.*, 205:523–552.

Kim, J., Kline, S. J., and Johnston, J. P., 1980. Investigation of a reattaching turbulent shear layer: Flow over a backward-facing step. *J. Fluids Eng.*, 102:302–308.

Koochesfahani, M. M. and Dimotakis, P. E., 1986. Mixing and chemical reactions in a turbulent liquid mixing layer. *J. Fluid Mech.*, 170:83–112.

Loehrke, R. I. and Nagib, H. M. Experiments on management of free-stream turbulence. Technical Report 598, AGARD, 1972.

Mungal, M. G. and Dimotakis, P. E., 1984. Mixing and combustion with low heat release in a turbulent shear layer. *J. Fluid Mech.*, 148:349–382.

Narayanan, M. A. B., Khadgi, Y. N., and Viswanath, P. R., 1974. Similarities in pressure distribution in separated flow behind backward-facing steps. *Aeronautical Quarterly*, 25:305–312.

Nie, J. H. and Armaly, B. F., 2003. Reattachment of three-dimensional flow adjacent to backward-facing step. *J. Heat Transfer*, 125:422–428.

Ötugen, M. V., 1991. Expansion ratio effects on the separated shear layer and reattachment downstream of a backward-facing step. *Exp. Fluids*, 10:273 – 280.

Ruderich, R. and Fernholz, H. H., 1986. An experimental investigation of a turbulent shear flow with separation, reverse flow, and reattachment. *J. Fluid Mech.*, 163:283–322.

Sinha, S. N., Gupta, A. K., and Oberai, M. M., 1981. Laminar separating flow over backsteps and cavities Part I: Backsteps. *AIAA Journal*, 19(12):1527–1530.

Slessor, M. D., 1998. *Aspects of turbulent shear-layer dynamics and mixing.* California Institute of Technology, Ph.D. thesis.

Su, W.-J., 2001. *Aerodynamic control of a subsonic diffuser.* California Institute of Technology, Eng. thesis.

Westphal, R. V. and Johnston, J. P., 1984. Effect of initial conditions on turbulent reattachment downstream of a backward-facing step. *AIAA Journal*, 22(12):1727–1732.

Yang, J.-T., Tsai, B.-B., and Tsai, G.-L., 1994. Separated-reattaching flow over a backstep with uniform normal mass bleed. *J. Fluids Eng.*, 116:29–35.

Yu, K. H., Wilson, K. J., and Schadow, K. C., 2001. Effect of flame-holding cavities on supersonic-combustion performance. *Journal of Propulsion and Power*, 17(6):1287–1295.